Distinguishing Mineral Oil Slicks From Low-Wind Areas Using Rapid-Repeat Synthetic Aperture Radar Imagery

Cornelius Patrick Quigley , A. Malin Johansson , *Member, IEEE*, Cathleen E. Jones , *Member, IEEE*, and Benjamin Holt , *Member, IEEE*

Abstract—A method for differentiating marine oil slicks from radar-dark, low-wind areas in open water using rapid-repeat synthetic aperture radar (SAR) imagery is reported. The study uses data acquired by the airborne NASA unmanned aerial vehicle SAR (UAVSAR) *L*-band SAR instrument, imaging the Coal Oil Point seep field near Santa Barbara, California. Time series of images from three different days are analyzed, all containing both verified oil slicks and low-wind zones. We propose a method to derive high-confidence oil/open water maps by exploiting the differences in spatial and temporal evolution between the low-wind zones and oil slicks over time scales of ∼1–3.5 h. Our method uses the standard deviation of the backscatter intensity for ensembles of colocated SAR pixels and is sufficiently simple and generic to be applied to near-real-time and without special processing code. The derived maps are compared with images of the ocean surface obtained by cameras mounted on a boat surveying the seep field simultaneously with the SAR. The imagery is manually classified into confirmed oil, likely oil, and open water classes. Our results show ∼1–7 dB difference between the SAR-derived mean standard deviation values of the confirmed/likely oil classes compared with the open water class. The minimum number of scenes needed to distinguish between areas of high likelihood of open water and oil slick was determined to be 3–5 scenes, spanning 50–80 min, depending on the spatial extent and persistence of the low-wind zones in the imagery.

Index Terms—Look-alike, low wind, oil spill, synthetic aperture radar (SAR), unmanned aerial vehicle synthetic aperture radar (UAVSAR).

I. INTRODUCTION

SYNTHETIC aperture radar (SAR) instruments have become vital operational tools for the identification and monitoring of mineral oil slicks in the marine environment. Presently, operational services engaged in the detection, characterization, and extraction of pertinent information regarding mineral oil spills, including their location, extent, and source, rely on the analysis of single-polarization spaceborne SAR imagery. These sensors are becoming increasingly utilized in guiding first responders to regions with actionable oil based on extracting features from individual SAR scenes, such as the damping ratio (DR) [1], [2], [3], [4], [5], [6], [7], [8], [9].

Mineral oil slicks are distinguishable in SAR imagery primarily because of smoothing of the ocean surface by the oil layer, which causes a reduction in the SAR backscatter [10]. As a result, mineral oil slicks can appear similar to other natural phenomena, often referred to as look-alikes, which exhibit a similar appearance [11], [12]. Some common look-alikes in addition to low-wind areas include natural biogenic surface films, shear zones, rain cells, and grease ice [11], [13]. Considerable attention has been placed on the case of natural biogenic slicks [14]. Large-scale experiments have been conducted at sea, where mineral oil, in conjunction with biogenic oil or oleyl alcohol, has been discharged [1], [15], [16], [17], [18]. Polarimetry was considered a promising approach for the differentiation of radar-dark features [17], [19], [20], [21], [22], [23], [24], [25], although it was later demonstrated that deviations in observed scattering mechanisms between different type of slicks were more likely attributed to internal system noise of the sensors [14], [26]. Recently, machine learning (ML) techniques have been proposed as a viable method to address the oil slick versus look-alike problem, where studies have been conducted on the efficacy of traditional ML techniques [27], [28], [29], [30] as well as the effectiveness of artificial neural network architectures of differing complexity for oil slick/oil look-alike discrimination [31], [32], [33], [34], [35], [36] with varying degrees of success.

However, the most ubiquitous oil spill look-alike phenomenon is associated with regions characterized by low-wind speeds. Unlike the previously mentioned look-alikes, low-wind zones are not confined to specific geographical locations and are less likely to be constrained by seasonal variations (e.g., increased biogenic activity during sunnier spring and summer months [37]). In addition, low-wind zones stand out as they are among the few phenomena that can generate regions of radar-dark pixels over ocean areas in SAR imagery even when there is no surface material present to dampen the surface capillary waves.

There are few studies in the literature that focus exclusively on separating surface mineral oil slicks from low-wind open ocean areas in SAR imagery. Two are [38] and [39], where both proposed algorithms for use in an operational setting to semiautomatically detect and classify radar-dark zones (oil slick or low wind) in ERS and Envisat ASAR imagery. However, both studies relied on auxiliary wind speed information. Bertacca et al. [40] proposed a method for classifying radar-dark areas into oil slick and low-wind areas in high-resolution SAR imagery without the need for auxiliary wind speed data. Their method was based on a fractionally integrated autoregressive-moving average model. However, their analysis was based on three ERS-1/2 SAR scenes, only one of which simultaneously contained low-wind areas and a verified mineral oil slick.

Nearly all the studies mentioned thus far, which focused on distinguishing mineral oil slicks from oil slick look-alikes, have used spaceborne SAR. However, airborne SAR sensors offer several advantages, such as the ability to be deployed to a specific area, rapidity of image acquisition, short repeat time imaging capability, and the potential of having a significantly higher signal-to-noise ratio (SNR) [41], [42].

The purpose of this study is to demonstrate that with repeat time series in the range of 1 h or less, distinguishing between areas containing oil slick and low-wind zones can be a highly tractable problem when using feature evolution. We analyze three separate time series acquired by NASAs *L*-band unmanned aerial vehicle synthetic aperture radar (UAVSAR) imaging the Coal Oil Point (COP) seep field off the coast of Santa Barbara, California, on three different days in June 2022. All scenes considered contain zones of verified oil slick and low-wind zones and were acquired as a part of the National Oceanic and Atmospheric Administration (NOAA)/NASA Marine Oil Spill Thickness Project.

Our proposed method utilizes the intensity variation in the sequence of SAR images to effectively identify the location of mineral oil slicks within a scene even in the presence of significant low-wind areas. We compare all derived high-confidence oil/open water maps to ground truth data provided by GoPro camera photos acquired from a boat within the seep field. Our proposed method is generic and adaptable enough to be easily implemented to providing quick results for responders.

II. STUDY AREA AND DATASET

The COP seep field is an area of natural seep activity of $\sim$13 km^2 extent [43] located in the Santa Barbara channel, California, which emits approximately 100 barrels of crude oil per day [44]. The sheltering effect from the outer channel islands and the proximity to Santa Barbara provide an ideal location to study oil slicks in low-wind and calm wave conditions.

The black rectangle in Fig. 1 indicates the area that was imaged by the UAVSAR on three low-wind days in 2022, namely 24, 28, and 29 June. The red, green, and blue lines in Fig. 1 indicate the boat tracks surveyed simultaneously to the UAVSAR acquired imagery. Fig. 1 also shows the locations of weather stations that measure wind speed and direction, and land-based
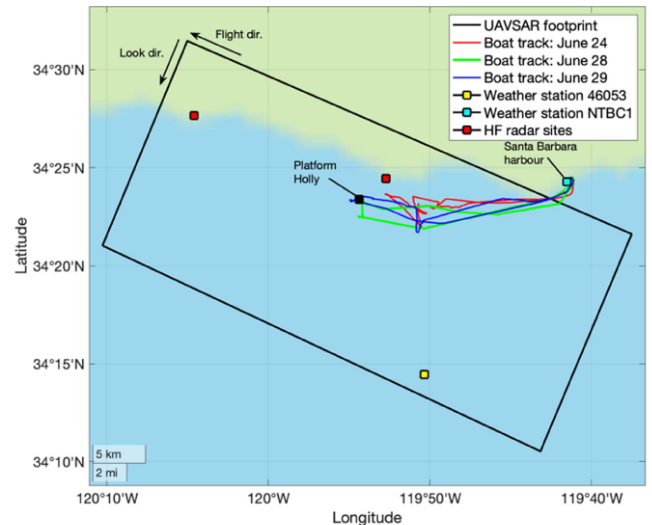

Fig. 1. Study area off the coast of Santa Barbara, California. Area imaged by the UAVSAR indicated by the black rectangle. Boat tracks are indicated by the red, green, and blue lines. Wind speed and direction taken from weather buoys marked by yellow and cyan points. HF Doppler radar sites marked in red.

TABLE I
UAVSAR ACQUISITION PERIOD AND TOTAL NUMBER OF ACQUISITIONS IN EACH TIME SERIES

Series ID	Time period (UTC)	No. of scenes	Time between acquisitions (min.)
24 June 2022	17:18 − 20:35	11	18−29
28 June 2022	17:22 − 18:32	5	17−18
29 June 2022	18:07 − 20:47	10	17−20

high-frequency (HF) Doppler radars that measure ocean surface current speed.

A. UAVSAR Data

The primary instrument used in this study is UAVSAR, an airborne *L*-band SAR in NASAs suite of airborne science instruments [45]. It offers the benefits of fine resolution (2 m slant range resolution) and short repeat time between scenes. It has a range swath width of 22 km, corresponding to an incidence angle range of $\sim$17°–67°. For ocean applications, the scene is cropped in the far range (62°) to avoid low SNR and cropped in the near range (25°) to be more sensitive to surface roughness [45]. All UAVSAR data used in this study are calibrated, georeferenced, ground range detected products, which are provided already multilooked by 3 (slant range) × 12 (azimuth) pixels. No additional averaging is done. As UAVSAR data have a high SNR due to their low instrument noise equivalent sigma zero (NESZ) (−47.8 dB at midrange) [45], no denoising was performed on the imagery used in this study. The images were acquired in the same flight pattern (imaging geometry), making the images directly comparable.

Table I presents relevant information for the time series acquired on 24, 28, and 29 June, and Figs. 2, 3, and 4 show all acquisitions used in this study. Radar-dark areas are present in all the time series. The wind conditions in relation to scene
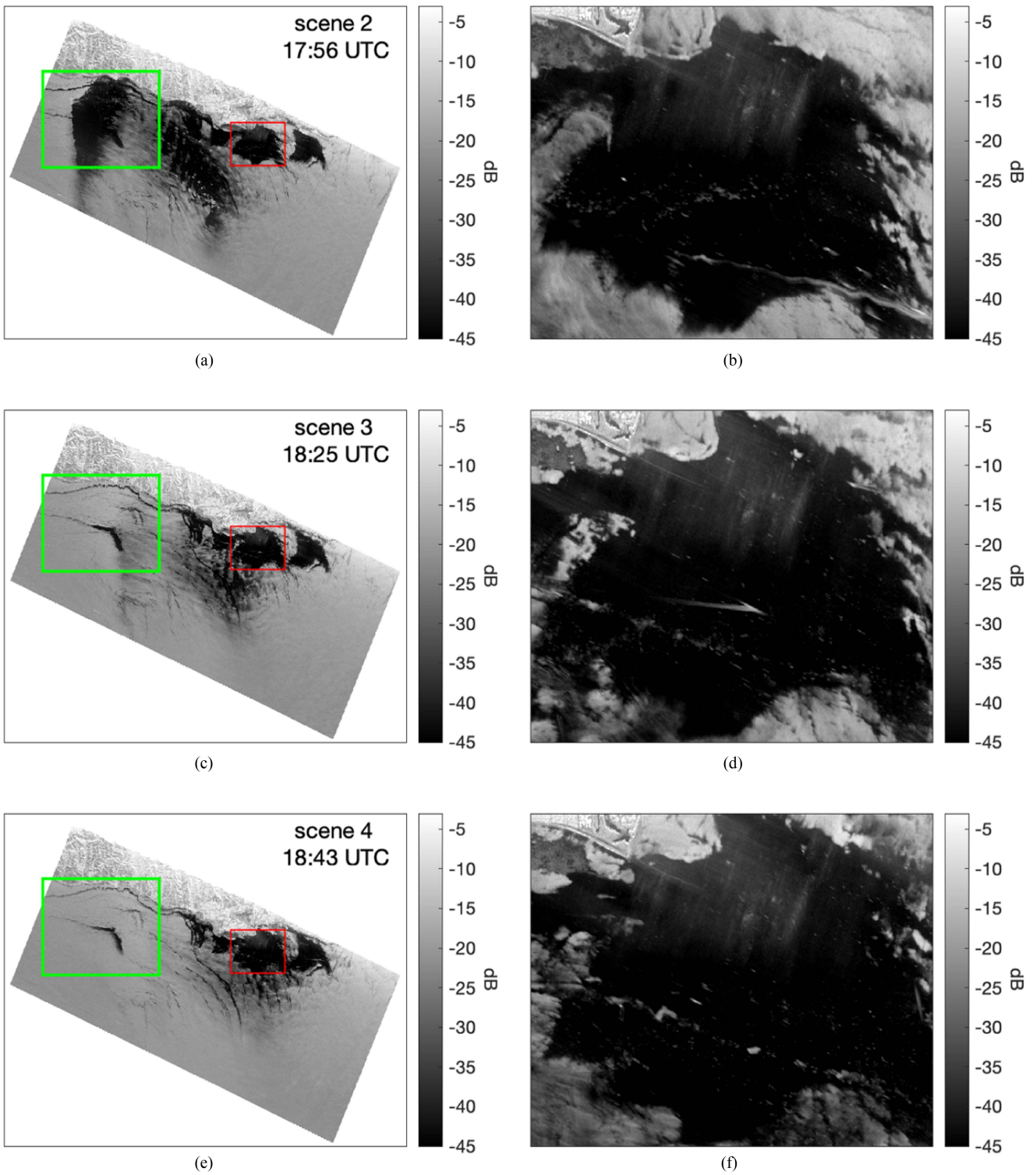
Fig. 2. (a), (c), and (e) VV-intensity images for scenes 2–4 acquired on 24 June 2022. An area of low wind, indicated by a radar-dark patch, can be seen traversing the imagery from the far left/middle of the scene to the right side of the scene throughout the time series. The red ROI shows where the boat was during the times these scenes were acquired. Two streamers are outlined by the green ROI. (b), (d), and (f) are zoomed-in on the red ROI in (a), (c), and (e), respectively.

Fig. 3.   (a)–(e) VV-intensity images for all scenes acquired on 28 June 2022. Scenes contain areas of both oil slick and low wind. The low-wind zones cover most of the image in (c)–(e).
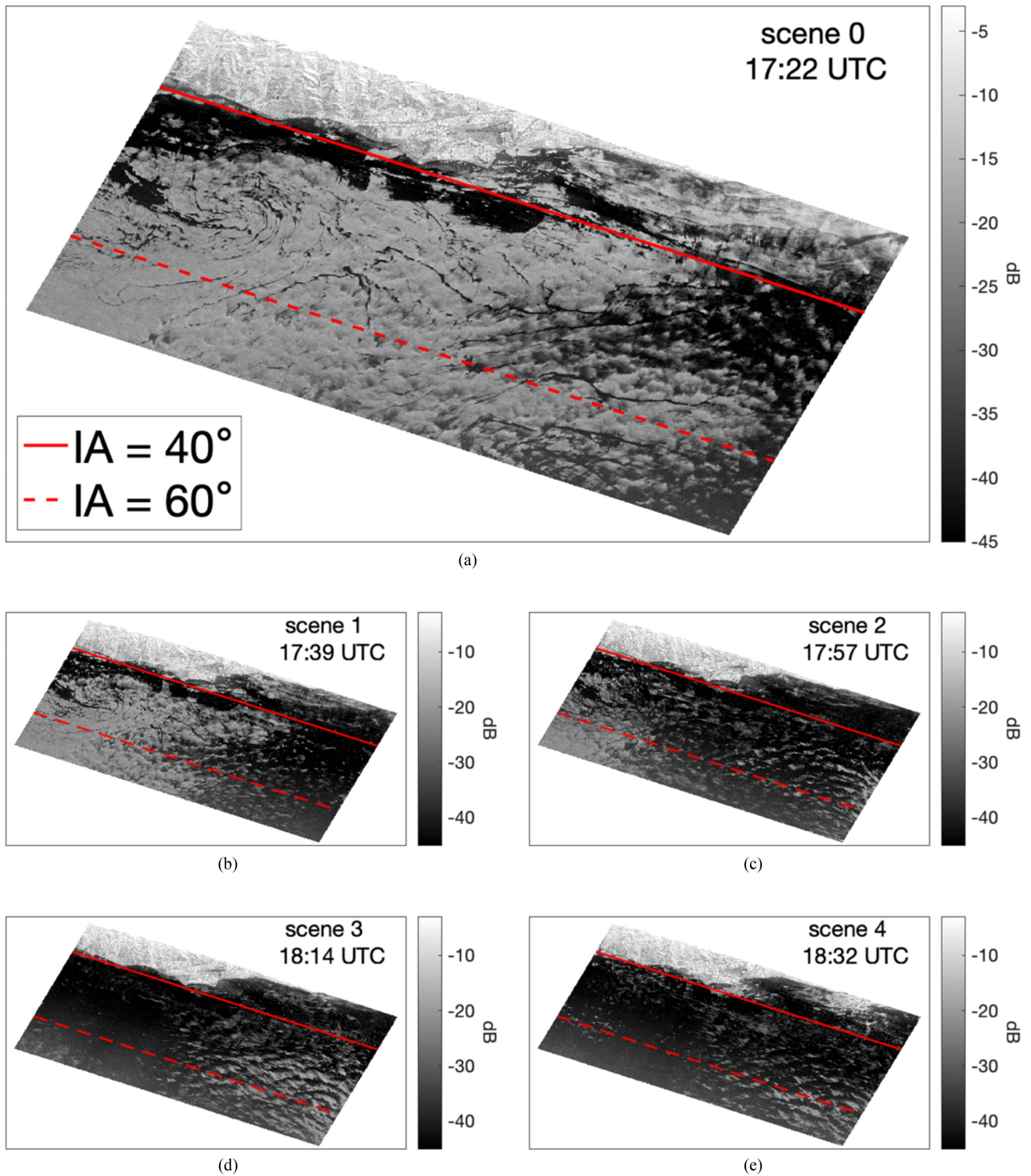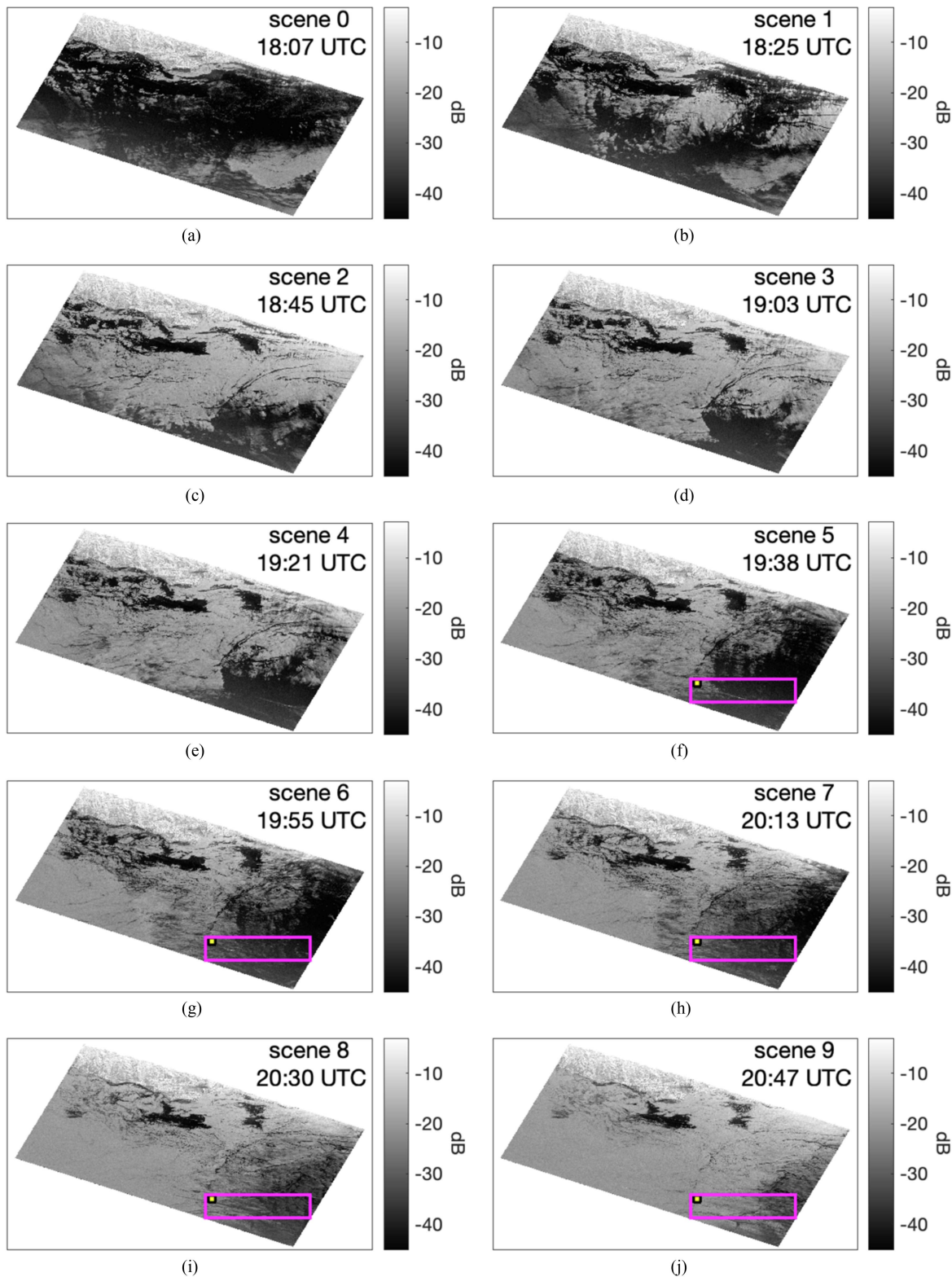
Fig. 4.   (a)–(j) VV-intensity images for all scenes acquired on 29 June 2022. Scenes contain areas of both oil slick and low wind. The 46053 weather buoys are marked by the yellow point. The purple rectangle outlines an area far from the seep field containing radar-dark zones believed to solely be areas of low wind. This area is used in the control experiment (see Section IV-C).

TABLE II
GoPro Video Acquisition Period and Number of Frames Used in This Study

Date and GoPro look direction	Time period (UTC)	Frames/ min	No. of frames used
24 June (right)	17:26 — 19:13	60	3814
28 June (right)	16:52 — 19:02	2	261
29 June (right)	18:07 — 20:47	2	322
29 June (left)	18:07 — 20:47	1	161

Some of the videos from 24 June were unrecoverable, and the gaps are shown in Fig. 5.

features are addressed in Section II-C. The 3 out of the 11 acquisitions from 24 June time series are used due to coincident low-wind conditions and the availability of in situ data during those acquisitions. The red region of interest (ROI) in Fig. 2 outlines the mineral oil slick area where the boat traversed. The green ROI outlines an area containing two thin slicks, which we call streamers, as discussed in Section IV. Figs. 3 and 4 show the acquisitions from 28 June and 29 June, respectively. The red lines in Fig. 3 indicate the incidence angle range 40°–60°, with smaller incidence angles to the north. Their relevance with respect to the NESZ is discussed in Section IV.

B. GoPro Data

In this study, we employ optical imagery acquired by boat-mounted GoPro cameras as validation data. Optical imagery was chosen, as oil slicks can be distinguished and variations in internal thickness can be discerned by visual appearance based on the Bonn Agreement Oil Appearance Code (BAOAC) [46]. In addition, GoPro cameras offer the advantages of being lightweight, cost-effective, easy to set up, can acquire high-definition imagery, are durable, and record all necessary auxiliary data, such as GPS coordinates and time stamp information. A camera setup that acquires images continuously ensures that human interference, which might bias the images toward oil slicks and not open water, is avoided. It should be noted, however, that imagery acquired by the GoPros may be susceptible to adverse weather conditions, such as glare caused by the sun or foggy conditions, and may result in the ocean surface being mischaracterized. This will be addressed in further detail in Section III-B.

Outward-facing GoPro cameras were attached to both sides of the boat (GoPro left/GoPro right) to document the sea surface conditions. Table II presents the details about the GoPro imagery, including the frame rate at which the imagery was recorded. On 28 June and 29 June, GoPro left and GoPro right were configured to acquire imagery at a rate of 2 frames/min and positioned 1 m above the water surface. GoPro left imagery is available for 29 June, at a rate of 1 frame/min, and on 24 June, GoPro right acquired continuous imagery at 1800 frames/min (30 frames/s), which were reduced to 60 frames/min to facilitate the analysis. The GoPro for 24 June was positioned 2.5 m above the water surface. When capturing imagery in this mode, GoPros are programmed to divide the resulting video into 12-min segments to prevent video corruption from causing loss of the entire footage. Unfortunately, three of these

video segments, which coincide with the UAVSAR acquisitions, suffered corruption and were unusable. These compromised video segments collectively amount to a total length of 36 min.

GoPro imagery starting from 30 min before the first UAVSAR acquisition and continuing until 30 min after the last acquisition was used for validation. GoPro images (each containing position and time metadata) were visually classified into oil/water classes, which facilitates validation of the high-confidence oil/open water radar maps. The classification scheme employed is described in Section III.

C. Wind Speed Data

Meteorology data are continuously measured from a network of weather buoys and stations in the Santa Barbara channel operated and maintained by the NOAA National Buoy Data Center. Wind speed and direction were obtained from the midchannel buoy 46053 and the shore station NTBC1 (see Fig. 1) and are available at 6- and 10-min intervals, respectively.

Wind speed and direction for the three days are shown in Fig. 5. The times of all UAVSAR acquisitions are indicated with vertical black lines, with those used in this study indicated by the black dots. The time extent of the GoPro imagery is outlined by the horizontal bars at the bottom of the graphs. Periods during which GoPro images were available are indicated in green and those in which GoPro images were unavailable are indicated in red. Five scenes are used in a control experiment to test the method on an area confirmed to be solely experiencing low wind in the absence of a mineral oil slick. These scenes are highlighted with pink squares [see Fig. 5(e)].

The 28 June UAVSAR imagery was most affected by radar-dark features that appear to be low-wind zones (see Fig. 3). Fig. 5(c) shows that the midchannel station registered very low-wind speeds of 1 m/s throughout the UAVSAR acquisition period. The shore-based station registered slightly higher wind speeds of about 1.2–1.8 m/s for the first four scenes and a wind speed of just under 3 m/s for the last scene. The area around the shore-based station for the first four UAVSAR scenes [see Fig. 3(a)–(d)] contains extensive radar-dark zones, and in Fig. 3(e), this area becomes radar bright, consistent with the presence of higher wind speeds.

The wind speed data for 29 June [see Fig. 5(e)] shows a general increase in the measured wind speed over the UAVSAR acquisition period. The shore-based station consistently measured values greater than 2 m/s while the midchannel buoy registered wind speeds less than 2 m/s for all scenes except the last one (4 m/s). The UAVSAR imagery in Fig. 4 also shows this trend with all scenes displaying more brighter pixels as time progresses. The areas around the midchannel buoy also contain radar-dark pixels in all scenes except the last.

The 24 June time series stands out because low-wind zones are highly localized within the UAVSAR imagery, not as widely distributed as on 28 or 29 June. Starting in scene 2 [see Fig. 2(a)], only the westmost portion of the scene contained low-wind zones, which then progressed in an eastward direction toward the shore station while missing the midchannel buoy [see
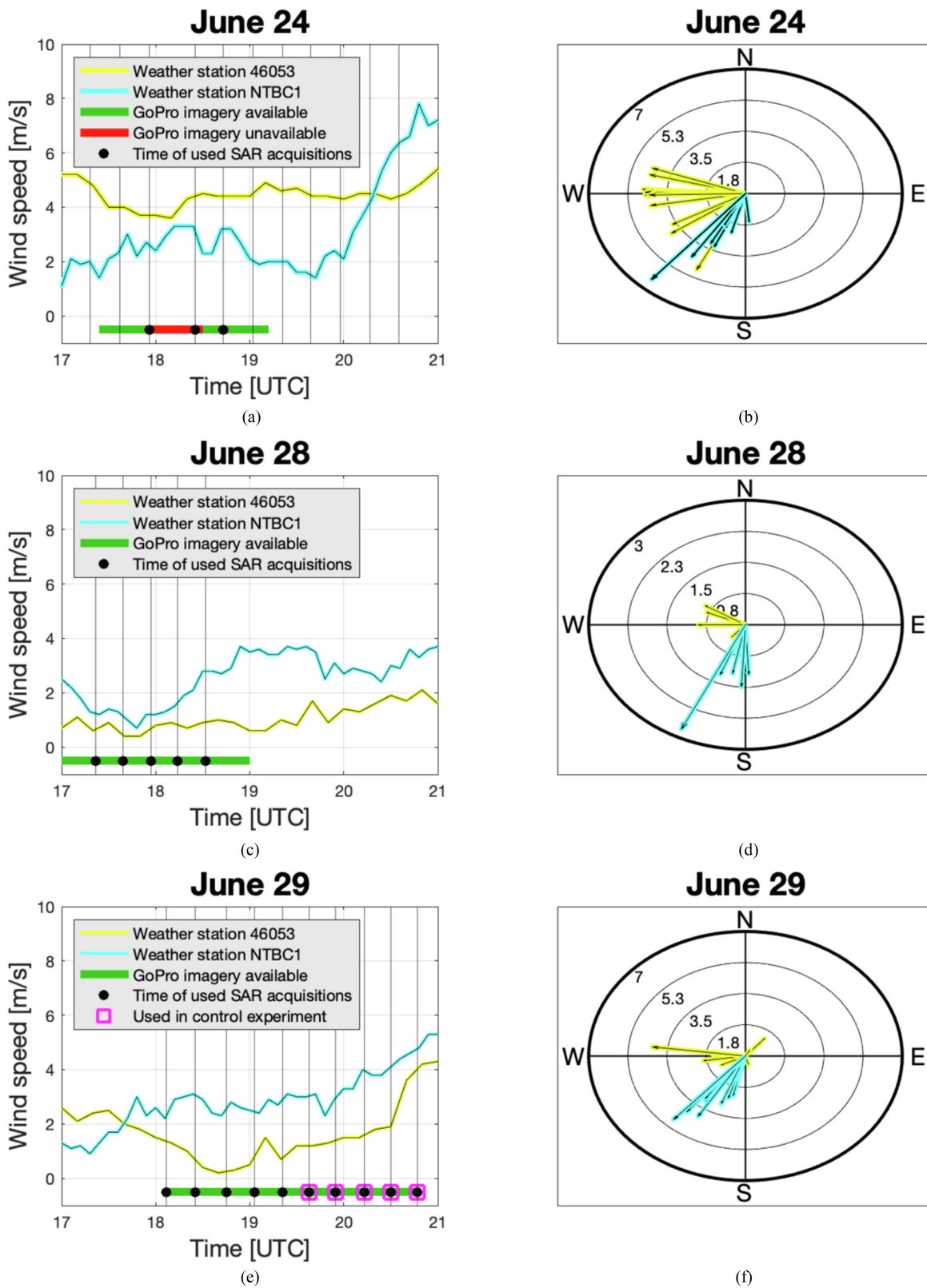
Fig. 5. (a), (c), and (e) show the measured wind speed versus time at the two weather stations, as shown in Fig. 1. The times of all UAVSAR acquisitions on each day are indicated by the vertical black lines, and the acquisitions used in this analysis are indicated with black dots. The purple boxes indicate acquisitions that are used in the control experiment. The time extents of the GoPro imagery are indicated by the horizontal green (available) and red (unavailable) lines. (b), (d), and (f) show the direction the wind came from, measured at the times of all UAVSAR acquisitions. The concentric circles indicate the magnitude of the wind speed in m/s.
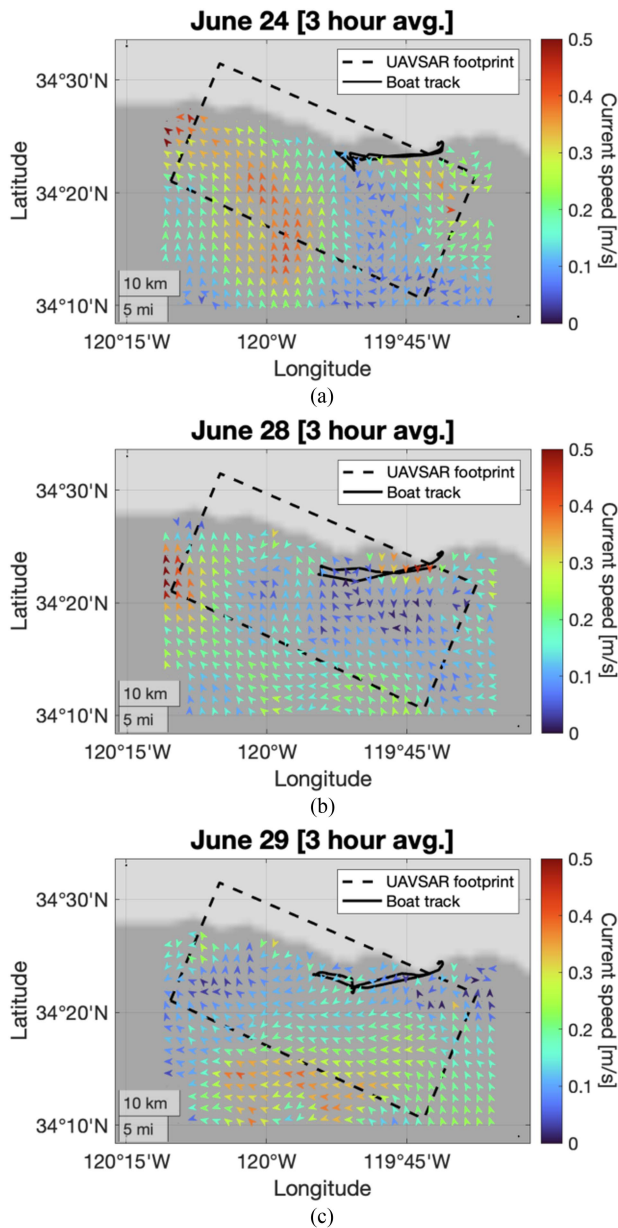
Fig. 6. Average surface current velocity at 2 km resolution from shore-based HF radars, measured over a period of 3 h corresponding to the acquisition time of the UAVSAR. The UAVSAR swath (dashed line) and the boat tracks (solid black lines) are indicated.

Fig. 2(c) and (e)]. The wind speed data in Fig. 5(a) confirms this trend with the midchannel buoy registering consistently higher wind speed than the shore-based station.

D. HF Radar Data

Land-based HF Doppler radars are located along the continental U.S. coast to measure surface current velocity. The HF radar network is operated and maintained by NOAA and is a component of their integrated ocean observing system [47], [48]. The locations of two of the radars used for this study are shown in Fig. 1. Fig. 6 displays their 3-h average ocean surface current speed and current direction at the time of the UAVSAR
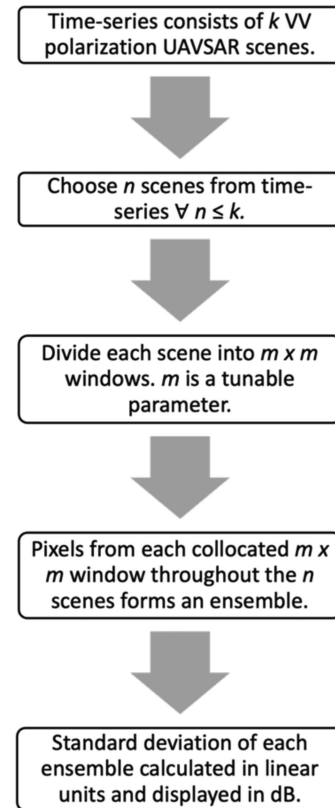

Fig. 7. Flowchart diagram of the proposed method.

acquisitions. The HF system provides the current velocity of the top $\sim$ 0.5–1 m of the ocean surface [48]. Velocities are averaged on an hourly basis and provided on a 2-km grid. The velocity speeds and directions in Fig. 6 are quite variable on each day, characteristic of the submesoscale circulation and variable winds found in this area [47].

Surface-dwelling slicks have been found to be transported at approximately 3% of the wind velocity and 100% of the current velocity [49]. Assuming a minimal influence of wind on oil drift in this scenario and using the range of measured current velocities, i.e., 0.08–0.43 m/s (24 June), 0.03–0.37 m/s (28 June), 0.08–0.23 m/s (29 June), the amount of drift experienced by any oil slicks present within the UAVSAR imaging area can be estimated. Values for oil slick drift were estimated to be 226–1213 m for 24 June (three scenes), 126–1554 m for 28 June (five scenes), and 768–2208 m for 29 June (ten scenes).

III. METHODOLOGY

A. Algorithm Description

We begin by hypothesizing that a pixel that is radar dark due to the presence of a mineral oil slick in one scene will have a higher probability of being radar dark in subsequent scenes of a SAR time series when rapid-repeat imagery is collected. In contrast, a pixel that is radar dark due to low wind may or may not be radar dark in subsequent scenes due to varying winds. The proposed hypothesis assumes that an oil slick drifts only
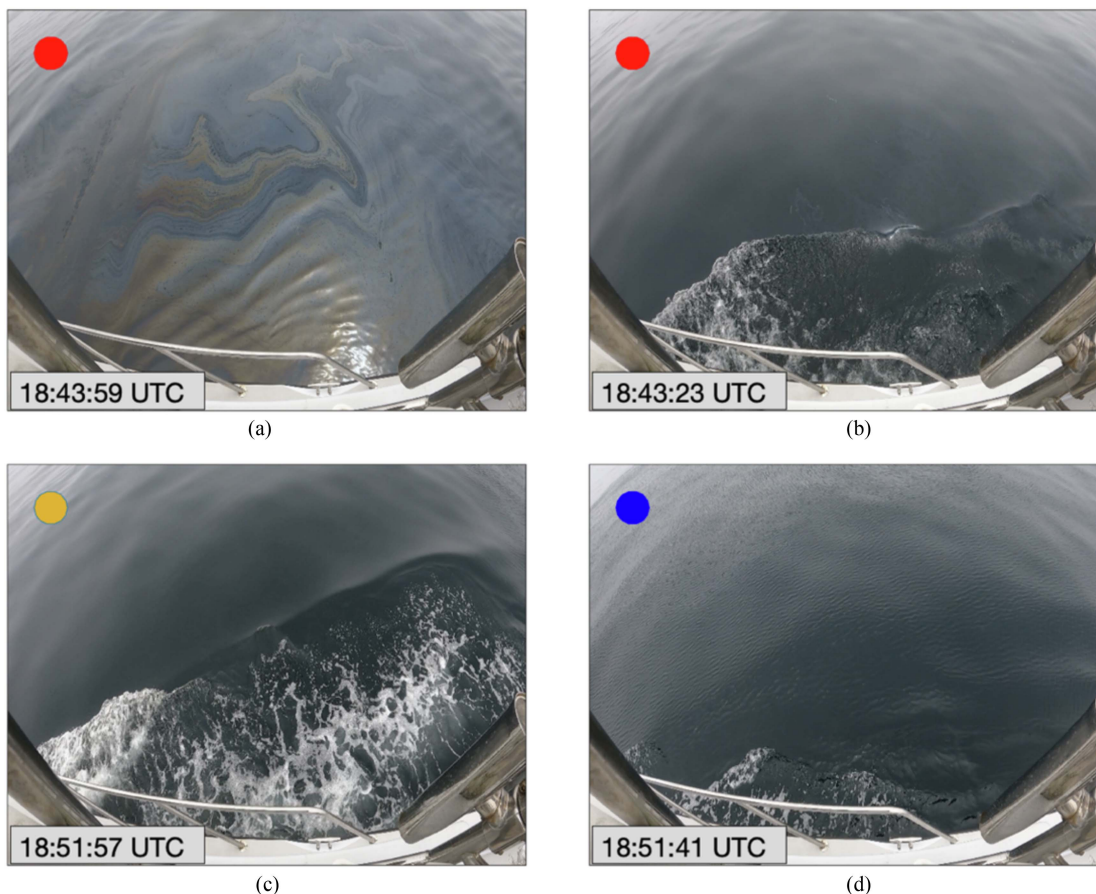
GoPro imagery: June 24

Fig. 8. Examples of classified GoPro images. (a) GoPro images with clearly visible oil are classified as confirmed oil and indicated with a red label. (b) A smooth, featureless surface with some indications of oil is also classified as confirmed (red), here seen as silver sheen in the very center of the image. (c) Smooth featureless surface with no other indications of oil is classified as likely oil, indicated by an orange label. (d) When small surface ripples characteristic of undamped capillary waves is observed, a blue label is applied indicating open water.

a short distance between acquisitions relative to the size of the imaged area.

In this study, we use the surface current speed data, as described in Section II-D, to illustrate that the imaged oil does not experience a significant amount of drift over the time frame of the UAVSAR data acquisitions. As stated in Section II-D, it was estimated from the surface current information within the UAVSAR footprint that the maximum oil drift values were approximately 1.2 km (on 24 June), 1.5 km (on 28 June), and 2.2 km (on 29 June). Although these values may appear substantial, they are small on the scale of the UAVSAR footprint. Therefore, relatively large oil slicks will have a substantial degree of overlap in the images during the acquisition period. In addition, more typical drift distances are around 280 m, 420 m, and 960 m for 24 June, 28 June, and 29 June, respectively, at a drift speed of 0.1 m/s.

An important aspect of the time-series SAR data is that they are georeferenced, so a pixel with image coordinates (i, j) is coregistered in all scenes. We begin by considering a time series consisting of k scenes in total, where n scenes are chosen by the user such that $n \leq k$. In this study, we assume that each of the n

scenes used were acquired successively. This will ensure the oil slick drifts only a short distance across the n scenes.

Here, each of the n SAR scenes is divided into square windows of size $m \times m$, where m is a tunable parameter. The standard deviation is calculated from an ensemble of pixels obtained by combining each collocated square window across the n scenes. If an $m \times m$ window corresponds to a geographic area containing an oil slick, then all pixels from the ensemble are expected to be radar dark and so will have a low standard deviation. In contrast, if all pixels in the ensemble are from radar bright open water, the standard deviation is expected to be larger. An $m \times m$ window corresponding to a region of open water experiencing low wind is expected to have an intermediate standard deviation value. However, as more scenes are incorporated, the standard deviation values are expected to converge toward that of radar bright open water. All standard deviation values are displayed in dB to improve interpretability.

The m parameter was set to values ranging from 3 to 21 with comparable results. However, employing larger values had the effect of spatially downsampling the final high-confidence oil/open water map and, thus, reducing its resolution. A value of
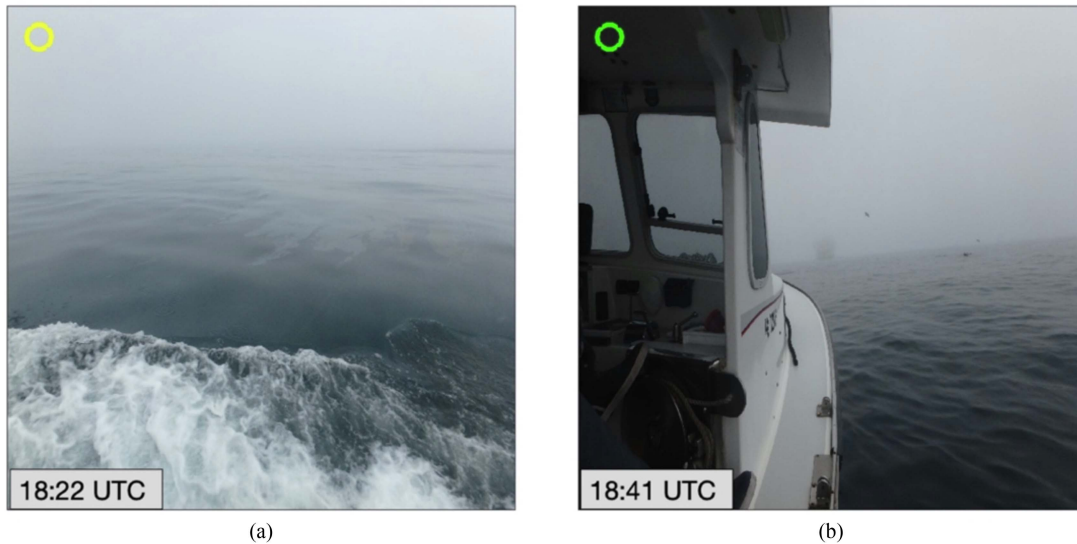
Fig. 9. Photographs taken from the boat with a handheld camera. (a) Boat is in an area of thin oil, where the boundary of a thicker oil region is a short distance away. Glare obscures any features or color discontinuities of the slickened surface. (b) Boat is in an area of open water. Due to low wind and effect of fog, small surface ripples (indicative of open water) are more difficult to observe. The position of the photos in Fig. 13 is marked with the corresponding yellow and green circles.

9 was determined to be an optimal choice for the UAVSAR data because it offered a sufficiently large ensemble for obtaining the accurate statistical values while still avoiding excessive downsampling.

While this approach can be applied to any polarization normalized radar cross section (NRCS), the most suitable polarization mode for this purpose is VV (vertical transmit, vertical receive) due to the consistently higher backscatter returns in the VV channel, which offers a higher margin above the instrument's noise floor. Fig. 7 provides a flowchart diagram outlining the proposed method.

B. Validation Data: GoPro Imagery

Individual GoPro frames were manually classified into three classes based on the visual appearance of the ocean surface, red for *confirmed oil*, orange for *likely oil*, and blue for *open water* (see Fig. 8). Confirmed oil would manifest as either a silver/rainbow sheen or thicker oil types that has become emulsified. The likely oil classification is assigned if the ocean surface had a smooth and glassy appearance, with no apparent oil present. Open water is used when the ocean surface exhibited no signs of oil and featured textural details, such as surface ripples. Fig. 8 presents four GoPro images taken on 24 June, showing visual examples of the classes. The classification categories are denoted by the presence of red, orange, and blue circles in the upper left corner of each image.

When classifying the GoPro imagery, each frame was categorized solely based on the information contained within that specific photo's field of view. Contextual factors, such as classifications from previous or subsequent images, or the geographic location of testing (e.g., in a region with natural seep activity),

were not considered. Every GoPro photograph was classified irrespective of the boat's speed, potentially resulting in multiple photos from a single area if the boat was stationary.

In certain cases, a predominantly smooth, glassy surface was observed with minor patches of oil, mostly in the form of silver sheen, e.g., Fig. 8(b). In such scenarios, the image was categorized under the confirmed oil class. The rationale behind this choice was that the presence of even a small amount of oil was indicative of the smooth surface being primarily a result of oil, rather than another potential surfactant, such as natural biogenic material.

The ability to effectively differentiate between the open water class and the confirmed/likely oil classes was notably enhanced under relatively clear and sunny weather conditions, as was the situation on 24 and 29 June. In contrast, adverse weather conditions, such as heavy fog, presented additional challenges in the classification of the GoPro imagery, as was the case on 28 June. An example of foggy conditions on 28 June is shown in Fig. 9, where two photographs taken by a handheld camera (not the GoPros) are shown. Fig. 9(a) shows a picture of the boundary between an area of thicker (farthest from the boat) and thinner (closer to boat) oil, as evident by the discontinuity. The presence of fog causes a significant amount of glare that likely caused a large amount of GoPro imagery to be classified as likely oil (orange) instead of confirmed oil (red). Fig. 9(b) shows an area that is believed to be open water. However, due to the glare caused by foggy conditions, any small contrasting surface features that would indicate the presence of open water can potentially be washed out, giving the ocean surface a false, smoother appearance. These weather conditions resulted in GoPro imagery that would be classified as open water (blue) under better visual observation being classified as likely oil (orange).

TABLE III
CROSS CORRELATION BETWEEN GOPRO RIGHT (GP-R) AND GOPRO LEFT (GP-L)

GP-R / GP-L	Open water	Likely oil	Confirmed oil
Open water	58 (36 %)	11 (7%)	10 (6%)
Likely oil	7 (4%)	20 (12%)	5 (3%)
Confirmed oil	5 (3%)	6 (4%)	39 (24%)

Number of photographs falling into each class is presented. Total number of photographs in this instance is 161.

C. Cross Comparison of GoPro Imagery

Given that imagery from two GoPros is available for 29 June, it is possible to compare the classifications. The GoPro right images were halved to match the quantity of GoPro left images. Images with the closest time stamp to GoPro left (13 s apart) were chosen for comparison. The results are presented in Table III. Despite the time gap of 13 s between the compared images, a significant proportion, 54%, was acquired within 10 m of each other and the largest separation observed was ~100 m. The entries along the diagonal of Table III show that there is a high degree of agreement between the classifications derived from the two GoPros.

IV. RESULTS AND DISCUSSION

The following sections present the derived high-confidence oil/open water maps for the three UAVSAR time series and compare the SAR standard deviation values in the vicinity of the boat track with the GoPro classifications.

A. 24 June Time-Series

During the 24 June acquisitions, low-wind conditions were near shore and not persistent throughout the time series, as discussed in Section II-C. The ability to mask out low-wind damping is shown in Fig. 10, where (a) shows a large area of low wind in addition to two streamers [see Fig. 2(a), (c), and (e)]. Fig. 10(b) shows the corresponding high-confidence oil/open water map, where the area of low wind is not apparent while the likely oil slicks, i.e., the streamers, are clearly delineated. The standard deviation values corresponding to the streamers are higher than the surrounding open water area, which contradicts previous assertions that oil slick areas retain low standard deviation values over a time series. However, this is most likely due to a northward movement of the streamers, which are primarily oriented east–west, over the time frame during which the UAVSAR images were acquired. Considering the elongated shape of the streamers, this could lead to a lack of overlap in consecutive scenes, and consequently cause a substantial increase in standard deviation values.

Fig. 10(c) displays DR masks from scenes 2 to 4, using a threshold of 1.2, here superimposed on each other. These two streamers exhibit a northward shift from scene 2 to scene 4, suggesting that drift is the probable factor contributing to the notably elevated standard deviation values. This is supported by the current speed data, as shown in Fig. 6(a), which shows
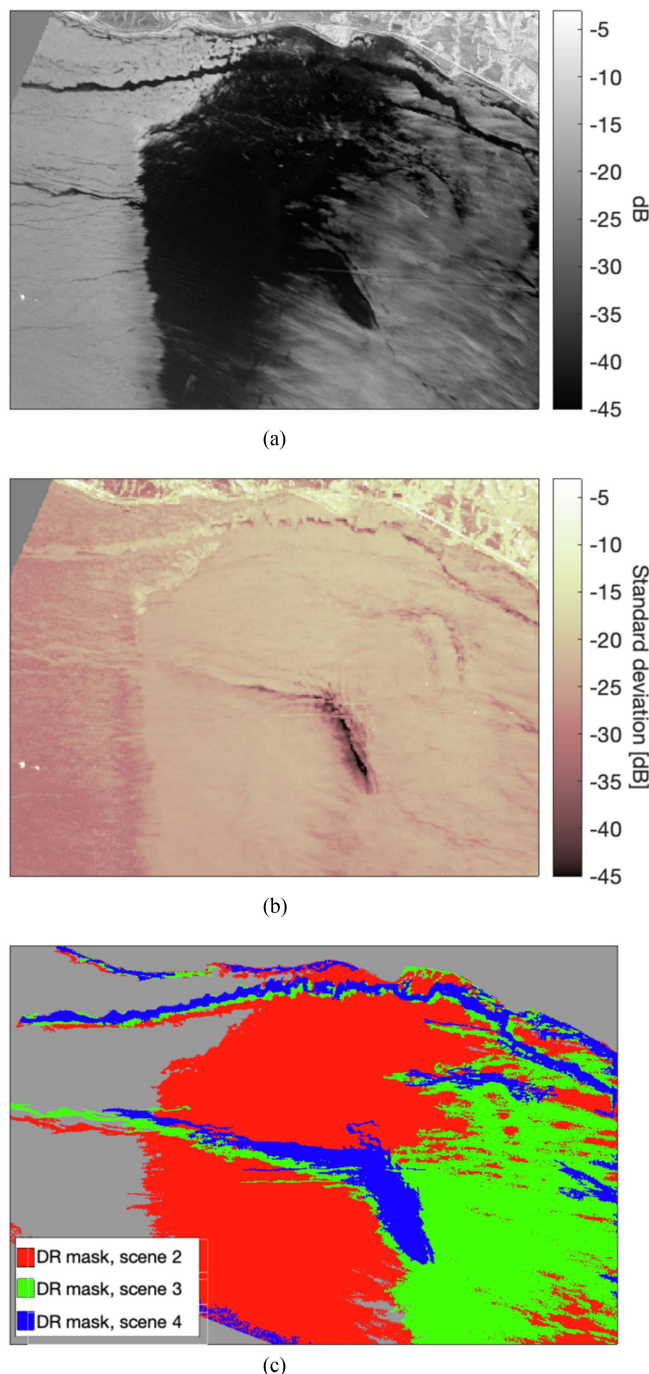

(a)

(b)

(c)

Fig. 10. (a) Green ROI in Fig. 2(a) (VV NRCS). (b) Corresponding high-confidence oil/open water map. (c) DR masks from three UAVSAR images.

northeast-bound currents (0.4–0.5 m/s) for this section of the scene. This suggests that identifying long, thin oil slick features within low-wind areas using time-series imagery may require a more nuanced interpretation.

Fig. 11(a) shows the high-confidence oil/open water map for the entire imaged area. Like Fig. 10(b), low standard deviation values more likely correspond to oil slick areas. Fig. 11(b) displays the red ROI in Fig. 11(a) and shows a dark region with clear boundaries, likely indicating the separation between oil slick and open water. This is the general area the boat traversed in
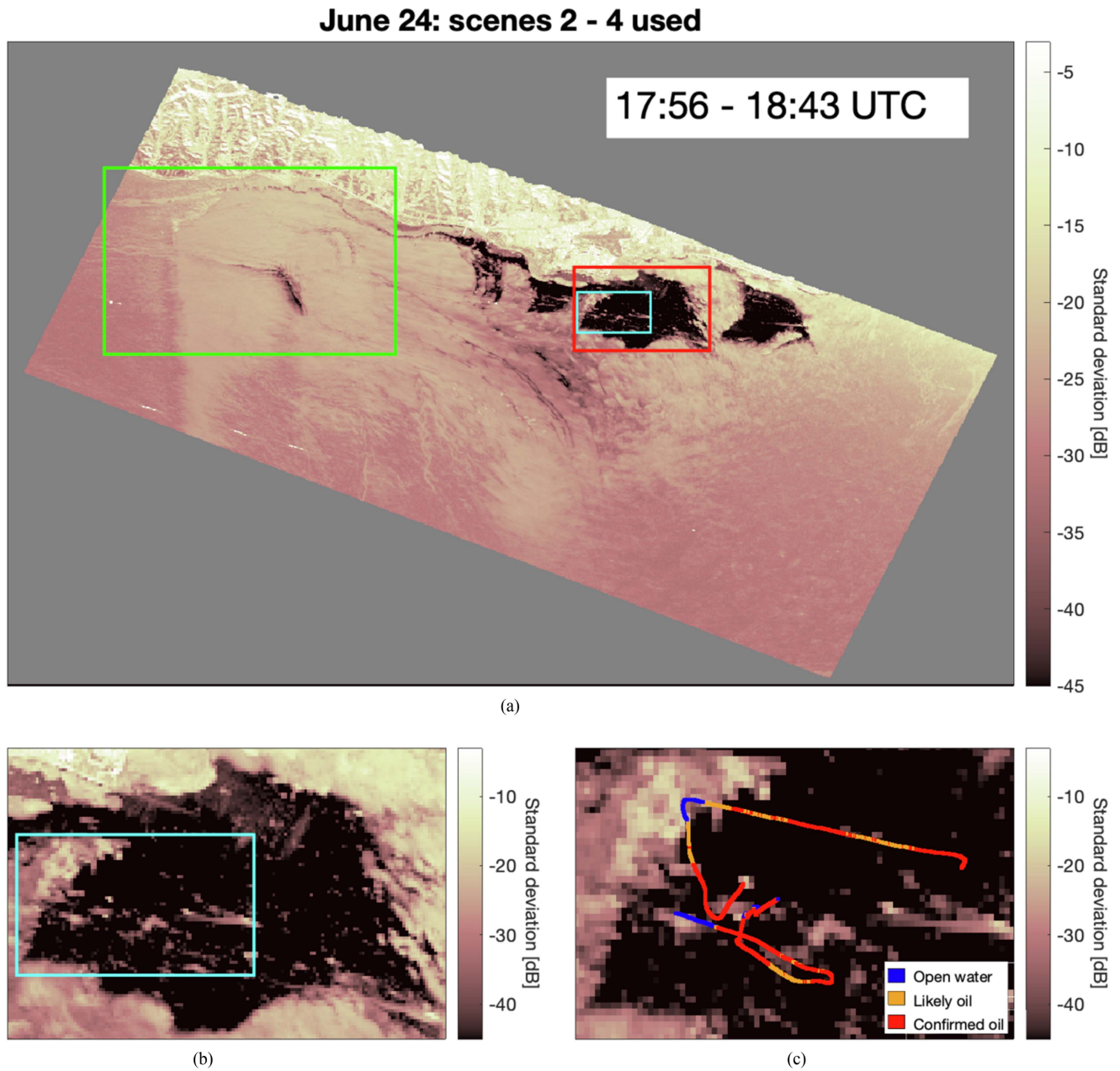
Fig. 11. (a) High-confidence oil/open water map for 24 June 2022, based on scenes 2–4. The low values (plotted as dark areas) are likely mineral oil slicks, while the high values (plotted as bright areas) are likely open (unslicked) water. (b) Area that corresponds to the red ROI in (a) is shown and the oil slick is a clearly delineated dark region with sharp borders. (c) Map for the smaller cyan ROI in (b) is shown as well as a classified boat track. Time extent for classified GoPro imagery is 17:26–19:13 UTC (SAR imaging time ±30 min).

the period corresponding to the three 24 June UAVSAR scenes. Fig. 11(c) shows the cyan ROI from Fig. 11(b). The boat track is overlayed and color coded based on the classification scheme, as introduced in Section III-B. The blue segments of track (open water) correspond to higher standard deviation values while the red and orange segments (confirmed/likely oil) correspond to lower standard deviation values. This observation is supported by Fig. 12(a), which presents a histogram of standard deviation values segregated by class for the boat track segment. The open water class exhibits higher average standard deviation values, with a difference of approximately 7 dB compared with the confirmed/likely oil classes.

B. 28 June Time-Series

As discussed in Section II-C, the time series on 28 June depicts an exceptional occurrence of very low-wind speed often covering the entire scene (see Fig. 3). This is further corroborated by the wind speed data, as illustrated in Fig. 5(c) and (d), where the recorded wind speeds at the times of the UAVSAR acquisitions were mostly below 2 m/s. Only the land-based station registered a wind speed >2 m/s at the time that scene 4 was acquired. In contrast, wind speed measurements during the UAVSAR acquisitions on 24 and 29 June frequently exceeded 3.5 m/s.
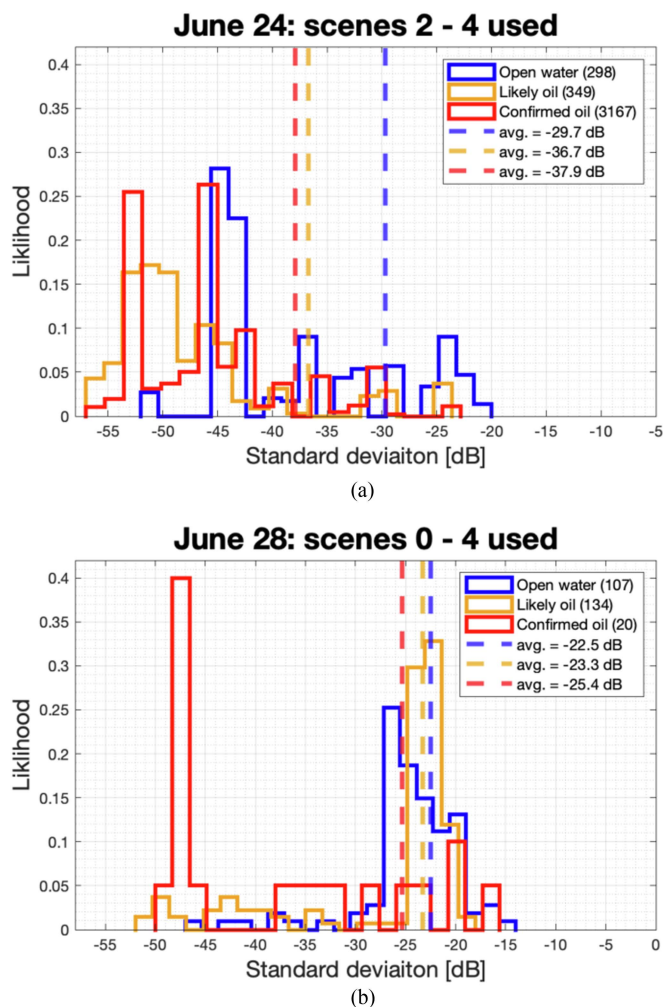
Fig. 12. Histograms of standard deviation values that correspond to the GoPro tracks for 24 June and 28 June separated by class. Number of GoPro images sorted into each class indicated in parentheses in the legend.

Upon visual examination of Fig. 3, it is apparent that scene 0 has the least low-wind zones, followed by scene 1, while scenes 2–4 exhibit a similar and more extensive occurrence of low-wind zoning. In this section, we create high-confidence oil/open water maps on a dataset that serves as an extreme example of how frequent low-wind conditions can entirely mask the presence of oil slicks in SAR imagery. This was done using three batches of imagery to evaluate the minimum number of images and time of observation needed to identify slicks under these conditions given the specific wind history.

Initially, all five scenes were used, then the process was repeated with all scenes except the first one (the scene with the least low-wind zoning), and finally using all scenes except the first two (both scenes with the least amount of low-wind zoning), thereby focusing on the three scenes within the time series most affected by low-wind zones. Fig. 13(a), (c), and (e) shows the resulting high-confidence oil/open water maps. The cyan ROI outlines the area the boat traversed over the period the UAVSAR images were acquired. As can be seen in Fig. 13(a) and (c), areas that are likely affected by oil slick are evident, characterized by their extensive and contiguous appearance.

In Fig. 13(e) (where only scenes 2–4 were used), the differentiation between regions likely to contain oil slick and open water becomes challenging, indicating that four scenes are a minimum requirement to separate these two classes for this dataset. We note that this number of scenes (time interval) depends upon the wind history, but this example shows that it is possible to identify mineral oil slicks using rapid-repeat imaging even in very low-wind conditions.

For validation of the method in this case, Fig. 13(b), (d), and (f) shows the area outlined by the cyan ROI along with the classified segment of the boat track. For Fig. 13(b) and (d), many of the blue open water segments are associated with higher standard deviation values, whereas the red confirmed oil segments are linked to lower standard deviation values.

As seen in Fig. 13(b) and (d), some sections of the boat track classified as orange (likely oil) are associated with both high and low standard deviation values. As discussed in Section III-B, the prevalence of both high and low standard deviation values corresponding to the orange class may be a result of the classification difficulties during the heavy fog on 28 June. The location of Fig. 9(a) is indicated by the yellow circle in Fig. 13(b), (d), and (f), an area characterized by predominantly low standard deviation values (indicating oil) and features an orange segment of track (likely oil), although the photograph is distinctly identified as an oil slick. In contrast, the green circle is placed in an area primarily exhibiting high standard deviation values (indicating the presence of open water) and, once again, features an orange segment of track (likely oil). As elaborated in Section III-B, this misclassification is likely attributable to glare from the fog, resulting in a disproportionate number of pixels being assigned to this intermediate class. This is also observable in Fig. 12(b), where the average standard deviation values for the open water, likely oil, and confirmed oil classes are −22.5 dB, −23.3 dB, and −25.4 dB, respectively, although the overlapping values between the blue and orange classes can be attributed to the inherent ambiguities introduced by foggy conditions. Despite the similarity in average values for all classes, the orange and red classes record lower standard deviation values than the blue class. Nonetheless, the limited availability of GoPro images during this period raises the possibility of low statistics affecting these results, leading to significant overlap within all classes.

Deriving the high-confidence oil/open water maps relies on the identification of sporadic bright patches in the radar image, as low-wind zones can move relatively rapidly across an area under investigation. Without these intermittent patches, the entire scene appears uniformly dark, leading to a lack of contrast throughout the scene. This scenario is illustrated in Fig. 13(e) and (f). Considering the persistent very low-wind conditions on 28 June, we assess whether a sensor characterized by an exceptionally low-noise floor, such as UAVSAR, was essential for this method to work or whether a sensor with a higher noise floor could have achieved the same objectives. This is relevant for the design of an airborne SAR instrument, specifically for oil spill response. The red lines plotted on the five UAVSAR images in Fig. 3 indicate the incidence angle bins of 40° and 60°. We extract backscatter values falling within the 95th to 99th percentile range for each incidence angle bin, in 1°
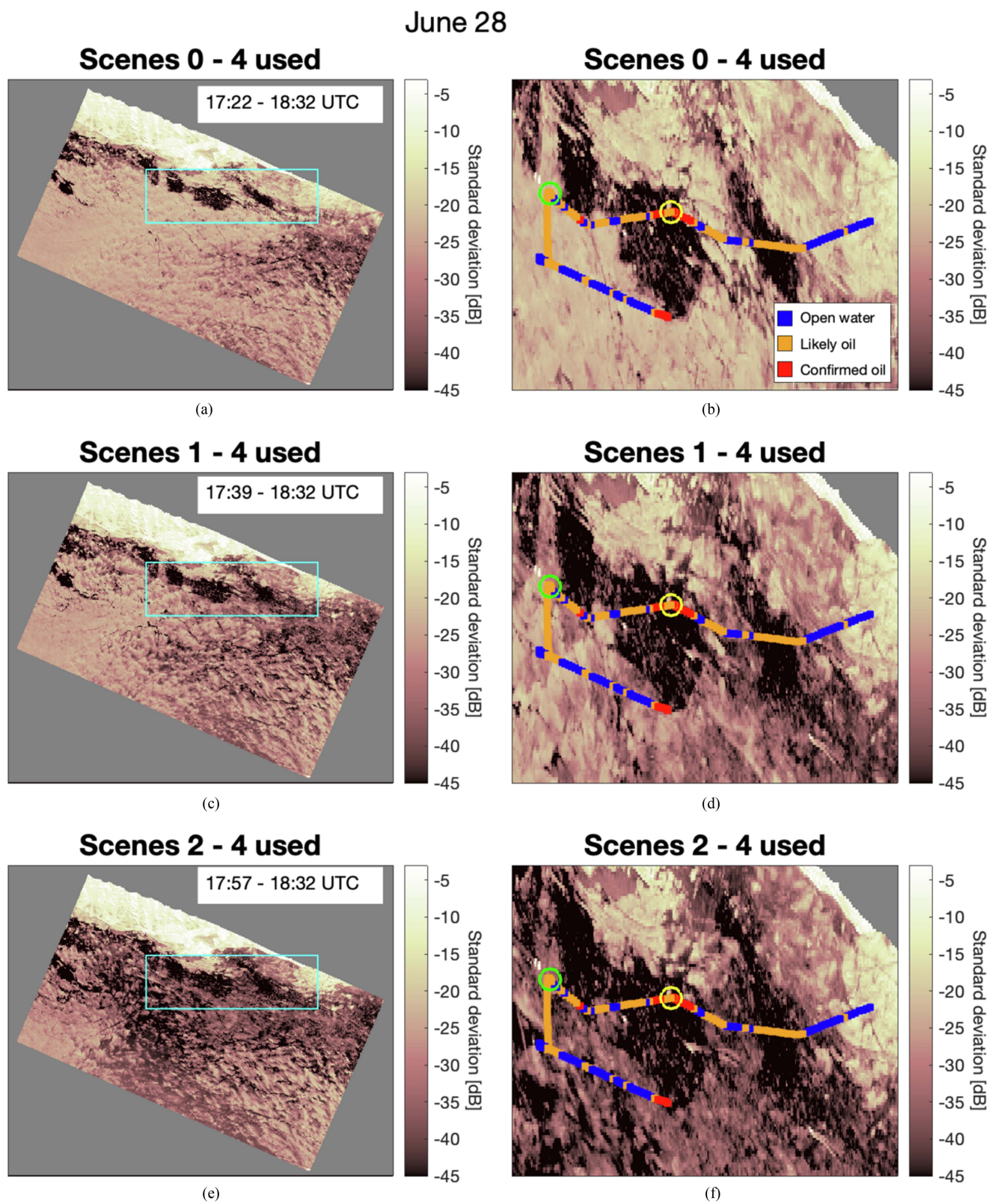
Fig. 13.   28 June high-confidence oil/open water maps for instances when (a) all five scenes of the time series are used, (c) first scene was excluded, and (e) first two scenes were excluded. The cyan box is an ROI that outlines an area where the boat traversed in which mineral oil slicks were present. (b), (d), and (f) show the cyan ROI from (a), (c), and (e), respectively, with classified GoPro imagery tracks. Time extent for classified GoPro imagery is 16:52–19:02 UTC (SAR imaging time ±30 min). The green and yellow circles indicate locations where the handheld photographs in Fig. 9 were taken.
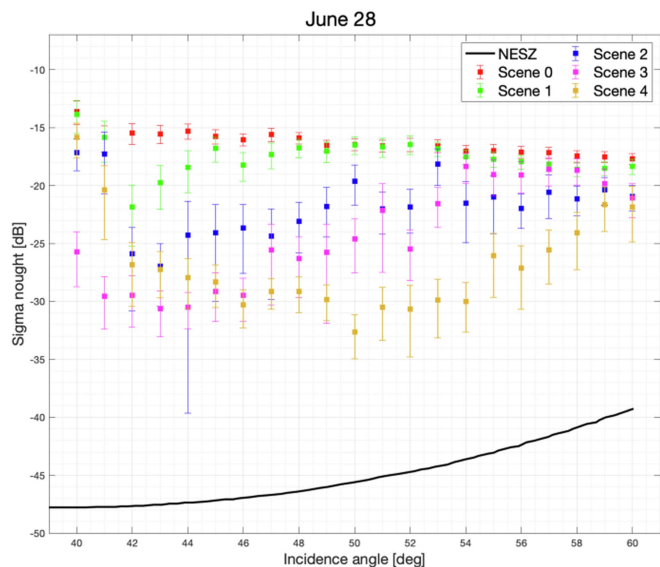
Fig. 14. Mean σ^0 values, ± 1 standard deviation (vertical bars), for the backscatter in the 95th–99th percentile, for each incidence angle bin between 40° and 60° for the five scenes in the 28 June time series. All mean values are at least 10 dB above the UAVSAR NESZ, as shown in black.

increments, and compute both the mean and standard deviation. This is done for each scene in the 28 June time series. The 100th percentile is intentionally omitted, primarily due to the probability that backscatter values at this level may be attributed to ships. This assumption is reasonable, considering that point sources representing ships are relatively small compared with the extent of the surrounding ocean.

The results are plotted in Fig. 14, where the black line is the noise equivalent sigma naught (NESZ) of the UAVSAR. As can be seen, all backscatter values are at least 10 dB above the noise floor of the sensor indicating that a less sensitive sensor could have yielded equivalent results.

C. 29 June Time Series (Control Experiment)

The analysis that was performed on the 24 and 28 June time series was similarly carried out on the 29 June time series. The 29 June is the longest time series considered in this study with ten scenes spanning 2 h and 40 min. It was investigated as to whether utilizing only half of the scenes can yield comparable results (i.e., scenes collected over an interval of 1 h and 20 min). Since the findings resemble those for the 24 and 28 June case, these results can be found in the Appendix.

Moreover, we test the method on an area of ocean, believed to be solely experiencing low-wind zoning, in the absence of oil slick. The area surrounding the 46053 weather buoy (see Fig. 1) was chosen for its distance from the COP seep field and the availability of localized wind speed information [see Fig. 5(e) and (f)] supporting our assertion that any radar-dark zones are likely due to low wind. This ROI can be seen as a pink box in Fig. 4(f) and (j). In addition, these five scenes were chosen as they were acquired in succession, a necessary requirement of the method (see Section III-A).
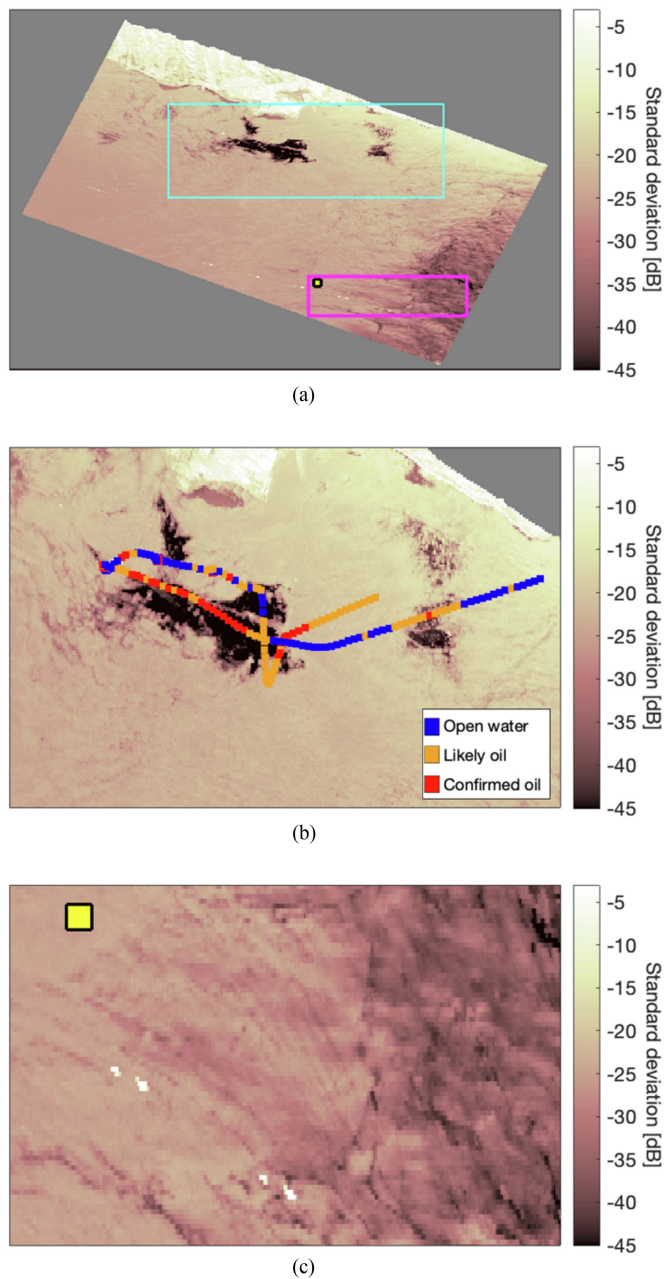

Fig. 15. (a) High-confidence oil/open water map for 29 June 2022, based on scenes 5–9. Blue ROI outlines area with what is believed to be oil slick. Pink ROI outlines area used in control experiment. The yellow dot is the weather buoy. (b) Blue ROI along with classified GoPro imagery tracks. (c) Pink ROI.

Fig. 15(a) shows the high-confidence oil/open water map for 29 June. A large, dark contiguous area, believed to be oil slick, is outlined by the blue ROI. The area surrounding the 46053 weather buoys (yellow square) is outlined by the pink ROI.

Fig. 15(b) shows the blue ROI from (a). The classified GoPro imagery tracks are superimposed onto the image. As can be seen, the dark, contiguous area, believed to be an oil slick, corresponds closely to the confirmed/likely oil classes, while the blue class corresponds to higher standard deviation values.

Fig. 15(c) shows the pink ROI. The very bright spots correspond to a boat that traversed the area while the scenes were being acquired. The left side of Fig. 15(c), nearest the 46053 weather buoys, has the largest standard deviation values that become progressively lower toward the right side of the ROI. The wind speed was measured to be continuously increasing from 1.2 to 4.0 m/s for scenes 5–9. In addition, the winds were measured to be blowing in a westward direction [see Fig. 5(e) and (f)]. This indicates that the right side of the ROI experienced a more severe degree of low-wind zoning than the left side.

While examining the blue and pink ROIs in Fig. 15(b) and (c), respectively, it is apparent that radar-dark zones that are a result of oil slick are likely to manifest as large contiguous areas, with relatively well-defined borders in the high-confidence oil/open water map. In contrast, radar-dark zones that are due to low wind are not as likely to manifest as contiguous zones and will tend to have higher standard deviation values closer to that of open water.

V. CONCLUSION

The primary objective of this study was to demonstrate the use of rapid-repeat airborne time series of SAR data to identify oil slicks in regions experiencing low-wind conditions, even when the radar-dark phenomena are colocated. We propose an automated approach that uses the standard deviation of the intensity across an entire time series of images, a method that can be readily implemented without the need for highly specialized code. Furthermore, the method we suggest eliminates the need for preprocessing steps, such as the computation of established and well-researched polarimetric features, such as the DR or co-polarization ratio. This is, especially, advantageous when dealing with situations where areas under investigation contain numerous radar-dark pixels concentrated within a single incidence angle bin in the azimuth direction, for which the former cannot be calculated [9].

The specific application of the method proposed is to separate mineral oil slicks from low-wind areas. In principle, any surfactant that responds to the ocean current and winds in a similar way to mineral oil will display low standard deviation values in the high-confidence oil/open water map. This means differentiating mineral oil and biogenic slicks using the method proposed is likely not possible. As a result, utilizing this method on SAR imagery in regions with high biological activity may lead to the inaccurate identification of a mineral oil slick. Thus, this method might be better suited for cleanup operations when there is clear and definite information about the existence of a slick, as opposed to its application in surveillance and monitoring operations.

However, differences in the time evolution between mineral oil and biogenic material, as observed in the SAR time series, may mitigate this issue. This would require a SAR with a high SNR to consistently obtain information on the internal state of the slickened material over a time series. Therefore, we recommend conducting airborne campaigns using a multifrequency SAR, such as DLRs airborne F-SAR, in the areas of high biological marine activity or oil-on-water campaigns where oil and biological material are discharged simultaneously [15], [16]. F-SAR can acquire simultaneous imagery in X-, C-, S-, L-, and P-bands, each with distinct noise floors [50].

One benefit, however, is that this method is expected to produce similar results for low-sulfur fuel oil spills. These are oils with low-sulfur content ($< 0.5\%$ by mass), which are required to be used for shipping operations (implemented by the International Maritime Organization) from January 2020 onward [51]. These oils have shown departures from the physical properties of other traditionally used fuel oils [51], indicating that applying well-established methods, such as the BAOAC [46], may be more difficult.

The high-confidence oil/open water maps presented in this study were derived from three time series of UAVSAR images, all of which showed some degree of low-wind zoning. The progression and distribution of low-wind areas were different on all three days, covering different low-wind scenarios. The maps were able to be derived from just 3–5 geolocated UAVSAR scenes, depending on the degree to which the scenes were affected by low wind. This amounts to approximately 50–80 min of imaging in the three cases examined. Considering the speed and straightforwardness of the method for computing the high-confidence oil/open water maps, it becomes feasible to execute this process onboard an aircraft and promptly provide results to first responders.

A unique aspect of this study involved employing GoPro imagery as truth data. Given our experience using both video and 1–2 frame/min captures, our recommendations for future use of this method are to use two or more GoPro cameras imaging different sides of the boat for redundancy and to collect video to provide more validation information. The GoPro imagery taken on 28 June was captured under foggy conditions, leading to the presence of glare. This likely resulted in imagery that should have been classified as confirmed oil (red) or open water (blue), being misclassified as likely oil (orange). Future experiments could add forward-looking infrared cameras to measure differences in the thermal emissivity between oil and water to better detect oil in foggy and poor lighting conditions.

As stated in Section III-B, areas of thicker slick may be over-represented in the classified GoPro imagery, as these areas were favored for collecting in situ data. However, typical drift values corresponding to the boat track were 0.1–0.2 m/s (see Fig. 6), meaning that, for 28 June and 29 June, the boat would have drifted between 30 and 60 m between successive GoPro photographs. Given that the boat has different drift characteristics than oil slick, it is unlikely that identical areas of slick were photographed. However, this is a possibility for the 24 June GoPro whose video was downsampled to a rate of 60 frames/min (0.1–0.2 m drift between frames). Our recommendations for future use of this method involve acquiring GoPro images from the boat moving fast enough to allow the cameras to consistently acquire images of different patches of the ocean surface. However, the speed should not be so fast as to create a bow wake, which will obscure any images acquired.

In this study, we used the mean of the standard deviation radar values to provide a simple statistical description of the histograms that correspond to the classified boat tracks

(see Fig. 12). The mean was used, instead of other well-established metrics, such as the median or the mode, because it is sensitive to extreme values, particularly for small samples' sizes. Therefore, the mean was expected to exhibit the lowest values for the confirmed oil class, intermediate values for the likely oil class, and the highest values for the open water class. This was observed for the 24 and 28 June time series (see Fig. 12) and the 29 June time series (see Appendix). It should be noted that this trend was observed for instances when a small amount of GoPro images was available (28 June) and when a relatively large amount of GoPro images was available (24 June). This indicates that regions with oil slick can be identified even in the presence of low wind with this method.

The 28 June time series was incorporated into this study to illustrate the application of the proposed method in a scenario where the entire scene is dominated by low-wind zones. As shown in Section IV-B, the highest backscatter values (95th–99th percentile) for 28 June were at least 10 dB above the noise floor of the instrument for a broad range of incidence angle values. This is significant, as it suggests high-confidence oil/open water maps can be obtained using a less sensitive instrument, which is a design consideration in SAR systems. However, it remains uncertain whether having information on the variability in intensity within an oil slick, measurable with a low-noise instrument, could contribute to the accuracy of the high-confidence oil/open water maps. Thus, we reiterate our prior recommendation that more multifrequency SAR studies acquiring data in different frequency bands with varying noise floors should be performed.

While this study shows promising results, it should be noted that persistent localized low-wind zones can lead to consistently low standard deviation values in the resulting high-confidence oil/open water map. This can be observed in the right-hand side of Fig. 15(a) and (c), where low standard deviation values in likely low-wind areas are indicated as open water in the high-confidence oil/open water. This may result in these low values being misinterpreted as oil slick. However, in the event of a massive spill, this potential issue may be mitigated because a single, large oil slick would manifest as a substantial, contiguous area characterized by low standard deviation values in the high-confidence oil/open water map. In the event of a smaller spill, where the slicks surface area might be similar in scale to the wind-induced, low standard deviation values in the high-confidence oil/open water map, identifying that the oil may prove more challenging and might require a more nuanced interpretation.

An essential requirement for the proposed technique in this study is the frequent and rapid imaging of areas with oil slicks, ensuring their positions overlap in subsequent imagery. Therefore, this method is well suited for airborne sensors. A notable advancement in recent years involves the emergence of microsatellite constellations by commercial providers.[1] These satellites most often operate in the X-band and have each orbit plane phased around the Earth, featuring different local times for

ascending and descending nodes rather than the more conventional dawn–dusk sun-synchronous orbit. This setup opens the potential for subdaily to daily rapid-repeat spaceborne imagery, particularly in higher latitudes. Although the X-band sensors tend to have higher noise floors relative to other frequency bands, the open ocean backscatter in the X-band is also generally higher. Thus, future work should also be conducted on the efficacy of applying this procedure to imagery from spaceborne SARs.

Appendix

In this appendix, we analyze the 29 June time series. We generated high-confidence oil/open water maps using the first five scenes, the last five scenes, and all scenes in the time series. We then compare the high-confidence oil/open water maps from all three combinations against the classified GoPro imagery for GoPro right. A total of 322 frames were obtained during the 2-h and 40-min period. To ensure a satisfactory number of GoPro frames for comparison, we compare the complete collection of GoPro imagery to all three combinations.

Fig. 16(a), (c), and (e) shows the high-confidence oil/open water maps derived using the first five scenes, the last five scenes, and all ten scenes in the time series, respectively. A large area of persistent oil can be seen in the top center of all three high-confidence oil/open water maps, outlined by a blue ROI. The bottom corner of the three high-confidence oil/open water maps shows moderately dark values, which are most likely due to persistent low-wind zoning in that region of the scene (see Fig. 4).

Fig. 16(b), (d), and (f) displays the blue ROI, and in all three images, the classified segments are overlaid. Again, the blue segments of the track (open water) are associated with higher standard deviation values, whereas the red segments (confirmed oil) correlate with lower standard deviation values. It should be noted that certain orange values (likely oil) align with higher standard deviation values. This reflects the challenges in manually classifying GoPro imagery, which can be susceptible to subjectivity.

Fig. 17 displays the histograms of standard deviation values categorized by class for the boat track segments in Fig. 16(b), (d), and (f). The average standard deviation values for open water are approximately -19 to -20.1 dB across all three scene batches, while for likely oil, they range from -20.2 to -21.6 dB. For confirmed oil, average values fall between approximately -22.7 to -23.3 dB.

Like the findings outlined in Section IV-A, the confirmed oil class consistently displays the lowest average standard deviation values, while the open water class consistently shows the highest average standard deviation values across all three dataset batches, although the separation between classes is not as pronounced as in the other time series. This difference is likely attributable to the significantly smaller number of available GoPro images on this date, with only 322 compared with the 3814 on 24 June. However, there is a notably higher occurrence of very low standard deviation values (< 40 dB) for the oil classes than for the open water class.

---

[1]See e.g. https://earth.esa.int/eogateway/missions/iceye# for a synopsis on the first SAR microsatellite. Last visited November 3, 2023.
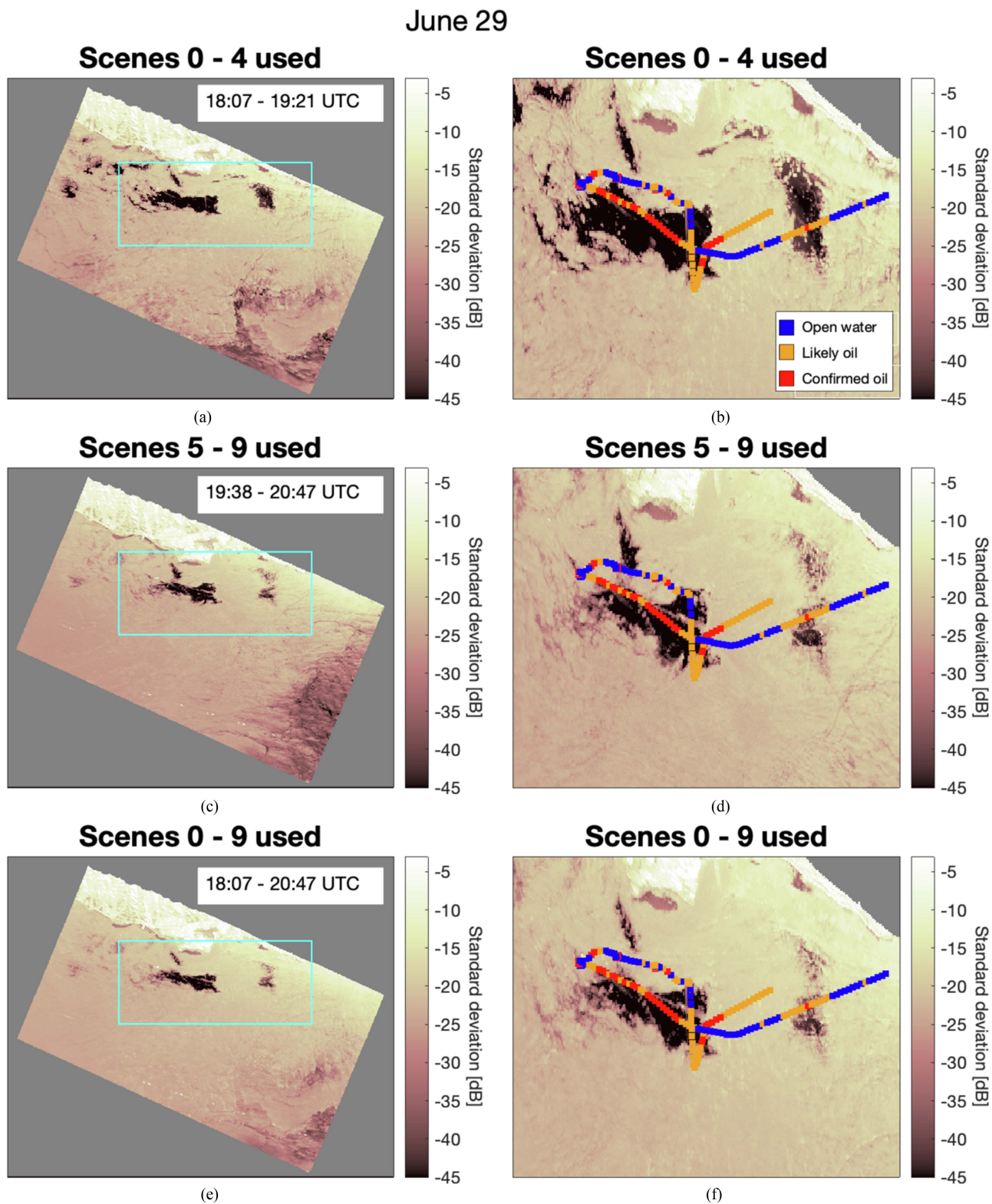
Fig. 16.   29 June high-confidence oil/open water maps for instances when (a) first five scenes of the time series are used, (c) last five scenes of the time series are used, and (e) all ten scenes in the time series are used. The cyan box is an ROI that outlines an area of what is believed to be mineral oil over which the boat traversed. (b), (d), and (f) show the cyan ROI from (a), (c), and (e) respectively. The classified GoPro imagery track is overlayed on these images and displayed in red, orange, and blue for the different classes. Time extent for classified GoPro imagery is 18:07–20:47 UTC.
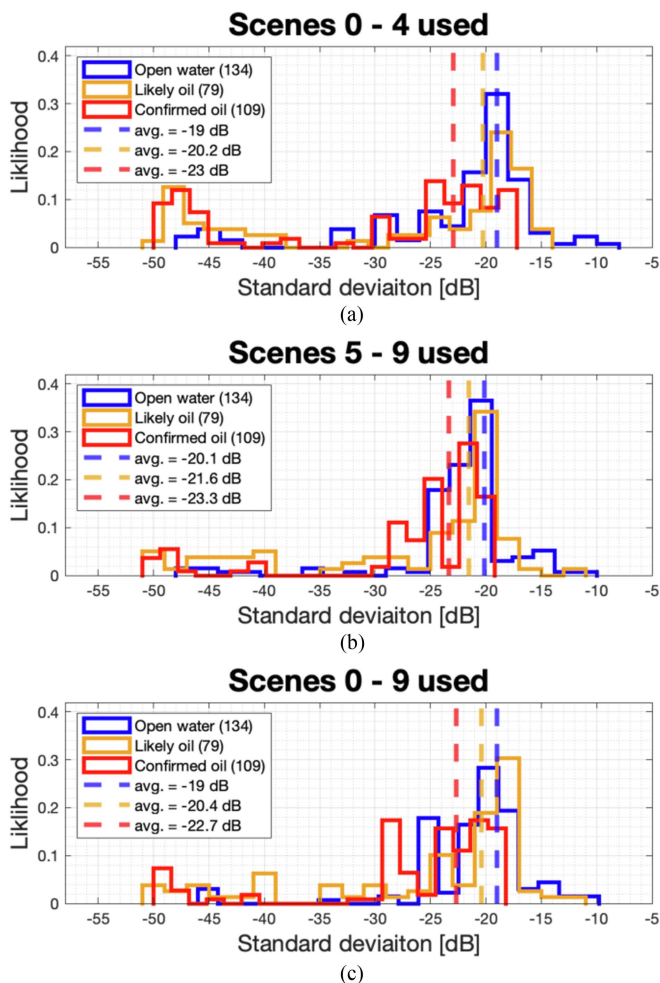
Fig. 17. (a)–(c) Histograms of standard deviation values that correspond to the classified GoPro tracks in Fig. 16(b), (d), and (f), respectively, divided by class. Average values for the likely oil class (orange) are between 1.2 and 1.4 dB lower than the average values for the open water class (blue). Average values for the confirmed oil class (red) are between 1.7 and 2.8 dB lower than the average values for the likely oil class (orange). Number of GoPro images sorted into each class indicated in parentheses in the legend.

ACKNOWLEDGMENT

REFERENCES

[1] M. Gade, W. Alpers, H. Huhnerfuss, H. Masuko, and T. Kobayashi, "Imaging of biogenic and anthropogenic ocean surface films by the multi-frequency/multipolarization SIR-C/X-SAR," *J. Geophysical Res., Oceans*, vol. 103, no. C9, pp. 18851–18866, Aug. 1998.

[2] M. Gade, W. Alpers, H. Huhnerfuss, V. Wismann, and P. Lange, "On the reduction of the radar backscatter by oceanic surface films: Scatterometer measurements and their theoretical interpretation," *Remote Sens. Environ.*, vol. 66, no. 1, pp. 52–70, Oct. 1998.

[3] B. Minchew, C. E. Jones, and B. Holt, "Polarimetric analysis of backscatter from the deepwater horizon oil spill using L-band synthetic aperture radar," *IEEE Trans. Geosci. Remote Sens.*, vol. 50, no. 10, pp. 3812–3830, Oct. 2012.

[4] V. Wismann, M. Gade, W. Alpers, and H. Huhnerfuss, "Radar signatures of marine oil spills measured by an airborne multi-frequency radar," *Int. J. Remote Sens.*, vol. 19, no. 18, pp. 3607–3623, Dec. 1998.

[5] S. Skrunes, C. Brekke, C. Jones, M. Espeseth, and B. Holt, "Effect of wind direction and incidence angle on polarimetric SAR observations of slicked and unslicked surfaces," *Remote Sens. Environ.*, vol. 213, pp. 73–91, Aug. 2018.

[6] O. Garcia-Pineda et al., "Classification of oil spill by thicknesses using multiple remote sensors," *Remote Sens. Environ.*, vol. 236, Jan. 2018, Art. no. 111421.

[7] D.-J. Kim, W. M. Moon, and Y.-S. Kim, "Application of TerraSAR-X data for emergent oil-spill monitoring," *IEEE Trans. Geosci. Remote Sens.*, vol. 48, no. 2, pp. 852–863, Feb. 2010.

[8] S. Skrunes, A. M. Johansson, and C. Brekke, "Synthetic aperture radar remote sensing of operational platform produces water releases," *Remote Sens.*, vol. 11, Dec. 2019, Art. no. 2882.

[9] C. E. Jones, "An automated algorithm for calculating the ocean contrast in support of oil spill response," *Mar. Pollut. Bull.*, vol. 191, Jun. 2023, Art. no. 114952.

[10] M. Fingas and C. Brown, "Review of oil spill remote sensing," *Mar. Pollut. Bull.*, vol. 4, no. 4, pp. 199–208, 1997.

[11] H. A. Espedal and O. M. Johannessen, "Detection of oil spills near offshore installations using synthetic aperture radar," *Int. J. Remote Sens.*, vol. 21, no. 11, pp. 2141–2144, Nov. 2000.

[12] A. H. S. Solberg, C. Brekke, and P. O. Husøy, "Oil spill detection in Radarsat and Envisat images," *IEEE Trans. Geosci. Remote Sens.*, vol. 45, no. 3, pp. 746–755, Mar. 2007.

[13] A. M. Johansson, M. M. Espeseth, C. Brekke, and B. Holt, "Can mineral oil slicks be distinguished from newly formed sea ice using synthetic aperture radar?," *IEEE J. Sel. Topics Appl. Earth Observ. Remote Sens.*, vol. 13, pp. 4996–5010, Aug. 2020.

[14] W. Alpers, B. Holt, and K. Zeng, "Oil spill detection by imaging radars: Challenges and pitfalls," *Remote Sens. Environ.*, vol. 201, pp. 133–147, Nov. 2017.

[15] M. M. Espeseth, S. Skrunes, C. E. Jones, C. Brekke, B. Holt, and A. P. Doulgeris, "Analysis of evolving oil spills in full-polarimetric and hybrid-polarity SAR," *IEEE Trans. Geosci. Remote Sens.*, vol. 55, no. 7, pp. 4190–4210, Jul. 2017.

[16] C. Brekke, M. M. Espeseth, K.-F. Dagestad, J. Rohrs, L. R. Hole, and A. Reigber, "Integrated analysis of multisensor datasets and oil drift simulations—A free-floating oil experiment in the open ocean," *J. Geophysical Res., Oceans*, vol. 126, no. 1, Dec. 2020, Art. no. e2020JC016499.

[17] S. Skrunes, C. Brekke, and T. Eltoft, "Characterization of marine surface slicks by Radarsat-2 multipolarization features," *IEEE Trans. Geosci. Remote Sens.*, vol. 52, no. 9, pp. 5302–5319, Sep. 2014.

[18] S. Skrunes, C. Brekke, and A. P. Doulgeris, "Characterization of SAR low backscatter ocean features using log-cumulants," *IEEE Geosci. Remote Sens. Lett.*, vol. 12, no. 4, pp. 836–840, Apr. 2015.

[19] M. Migliaccio, A. Gambardella, and M. Tranfaglia, "SAR polarimetry to observe oil spills," *IEEE Trans. Geosci. Remote Sens.*, vol. 45, no. 2, pp. 506–511, Feb. 2007.

[20] J. Yin, J. Yang, L. Zhou, and L. Xu, "Oil spill discrimination by using general compact polarimetric SAR features," *Remote Sens.*, vol. 12, no. 3, Feb. 2020, Art. no. 479.

[21] M. W. Hansen, V. Kudryavtsev, B. Chapron, C. Brekke, and J. A. Johannessen, "Wave breaking in slicks: Impacts on C-band quad-polarized SAR measurements," *IEEE J. Sel. Topics Appl. Earth Observ. Remote Sens.*, vol. 9, no. 1, pp. 4929–4940, Nov. 2016.

[22] F. Nunziata, A. Gambardella, and M. Migliaccio, "On the Mueller scattering matrix for SAR sea oil slick observation," *IEEE Geosci. Remote Sens. Lett.*, vol. 5, no. 4, pp. 691–695, Oct. 2008.

[23] S. Skrunes, C. Brekke, T. Eltoft, and V. Kudryavtsev, "Comparing near-coincident C- and X-band SAR acquisitions of marine oil spills," *IEEE Trans. Geosci. Remote Sens.*, vol. 53, no. 4, pp. 1958–1975, Apr. 2015.

[24] S. Tong, X. liu, Q. Chen, Z. Zhang, and G. Xie, "Multi-feature based ocean oil spill detection for polarimetric SAR data using random forest and the self-similarity parameter," *Remote Sens.*, vol. 11, no. 4, Feb. 2019, Art. no. 451.

[25] A.-B. Salberg, Ø. Rudjord, and A. H. S. Solberg, "Oil spill detection in hybrid-polarimetric SAR images," *IEEE Trans. Geosci. Remote Sens.*, vol. 52, no. 10, pp. 6521–6533, Oct. 2014.

[26] M. M. Espeseth, C. Brekke, C. E. Jones, B. Holt, and A. Freeman, "The impact of system noise in polarimetric SAR imagery on oil spill observations," *IEEE Trans. Geosci. Remote Sens.*, vol. 58, no. 6, pp. 4194–4214, Jun. 2020.

[27] L. Xu, J. Li, and A. Brenning, "A comparative study of different classification techniques for marine oil spill identification using RADARSAR-1 imagery," *Remote Sens. Environ.*, vol. 141, pp. 14–23, Feb. 2014.

[28] G. de Araujo Carvalho, P. J. Minnett, M. F. F. Ebecken, and L. Landau, "Machine-learning classification of SAR remotely-sensed sea-surface petroleum signatures—Part 1: Training and testing cross validation," *Remote Sens.*, vol. 14, no. 13, Jun. 2022, Art. no. 3027.

[29] Y. Cao, L. Xu, and D. Clausi, "Exploring the potential of active learning for automatic identification of marine oil spills using 10-year (2004–2013) RADARSAT data," *Remote Sens.*, vol. 9, no. 10, Oct. 2017, Art. no. 1041.

[30] M. R. A. Conceição et al., "SAR oil spill detection system through random forest classifiers," *Remote Sens.*, vol. 13, no. 11, 2021, Art. no. 2044.

[31] S. Singha, T. J. Bellerby, and O. Trieschmann, "Satellite oil spill detection using artificial neural networks," *IEEE J. Sel. Topics Appl. Earth Observ. Remote Sens.*, vol. 6, no. 6, pp. 2355–2363, Dec. 2013.

[32] O. Garcia-Pineda, I. R. MacDonald, X. Li, C. R. Jackson, and W. G. Pichel, "Oil spill mapping and measurement in the Gulf of Mexico with textural classifier neural network algorithm (TCNNA)," *IEEE J. Sel. Topics Appl. Earth Observ. Remote Sens.*, vol. 6, no. 6, pp. 2517–2525, Dec. 2013.

[33] J. Fan and C. Liu, "Multitask GANs for oil spill classification and semantic segmentation based on SAR images," *IEEE J. Sel. Topics Appl. Earth Observ. Remote Sens.*, vol. 16, pp. 2532–2546, Feb. 2023.

[34] D. Blondeau-Patissier et al., "Detection of marine oil-like features in Sentinel-1 SAR images by supplementary use of deep learning and empirical methods: Performance assessment for the great barrier reef marine park," *Mar. Pollut. Bull.*, vol. 188, Mar. 2023, Art. no. 114598.

[35] S. Singha and R. Ressel, "Offshore platform sourced pollution monitoring using space-borne fully polarimetric C- and X-band synthetic aperture radar," *Mar. Pollut. Bull.*, vol. 112, no. 1/2, pp. 327–340, Nov. 2016.

[36] L. De Laurentiis, C. E. Jones, B. Holt, G. Schiavon, and F. Del Frate, "Deep learning for mineral and biogenic oil slick classification with airborne synthetic aperture radar data," *IEEE Trans. Geosci. Remote Sens.*, vol. 59, no. 10, pp. 8455–8469, Oct. 2021.

[37] O. D. Beltran-Perez and J. J. Waniek, "Inter-annual variability of spring and summer blooms in the Eastern Baltic Sea," *Front. Mar. Sci.*, vol. 9, Aug. 2022, Art. no. 928633.

[38] H. A. Espedal, "Satellite SAR oil spill detection using wind history information," *Int. J. Remote Sens.*, vol. 20, no. 1, pp. 49–65, Jan. 1999.

[39] F. Girard-Ardhuin, G. Mercier, F. Collard, and R. Garello, "Operational oil-slick characterization by SAR imagery and synergistic data," *IEEE J. Ocean. Eng.*, vol. 30, no. 3, pp. 487–495, Jul. 2005.

[40] M. Bertacca, F. Berizzi, and E. D. Mese, "A FARIMA-based technique for oil slick and low-wind areas discrimination in sea SAR imagery," *IEEE Trans. Geosci. Remote Sens.*, vol. 43, no. 11, pp. 2484–2493, Nov. 2005.

[41] C. E. Jones and B. Holt, "Experimental L-band airborne SAR for oil spill response at sea and in coastal waters," *Sensors*, vol. 18, no. 2, Feb. 2018, Art. no. 641.

[42] M. M. Espeseth, C. E. Jones, B. Holt, C. Brekke, and S. Skrunes, "Oil-spill-response-oriented information products derived from a rapid-repeat time series of SAR images," *IEEE J. Sel. Topics Appl. Earth Observ. Remote Sens.*, vol. 13, pp. 3448–3461, Jun. 2020.

[43] I. Leifer, "A synthesis review of emissions and fates for the coal oil point marine hydrocarbon seep field and California marine seepage," *Geofluids*, vol. 2019, Oct. 2019, Art. no. 4724587.

[44] J. S. Hornafius, D. Quigley, and B. P. Luyendyk, "The world's most spectacular marine hydrocarbon seeps (coal oil point, Santa Barbara channel, California) quantification of emissions," *J. Geophys. Res.*, vol. 104, no. C9, pp. 20703–20711, Sep. 1999.

[45] A. G. Fore et al., "UAVSAR polarimetric calibration," *IEEE Trans. Geosci. Remote Sens.*, vol. 53, no. 6, pp. 3481–3491, Jun. 2015.

[46] Bonn Agreement Secretariat, "Bonn agreement aerial operations handbook," Tech. Info. Paper, London, U.K., 2016, Accessed on: Dec. 9, 2023. [Online]. Available: https://www.bonnagreement.org/site/assets/files/1081/aeriaa_operations_handbook.pdf

[47] R. H. Stewart and J. W. Joy, "HF radio measurements of surface currents," *Deep Sea Res. Oceanogr. Abstr.*, vol. 21, no. 12, pp. 1039–1049, Dec. 1974.

[48] A. R. Payandeh, L. Washburn, B. Emery, and J. C. Ohlmann, "The occurrence, variability, and potential drivers of submesoscale eddies in the southern California bight based on a decade of high-frequency radar observations," *J. Geophysical Res., Oceans*, vol. 128, no. 10, Oct. 2023, Art. no. e2023JC019914.

[49] ITOPF, "Aerial observation of marine oil spills," Technical Information Papers (TIP), London, U.K., ITOPF Tech. Rep. 1, 2011, p. 12.

[50] A. Reigber et al., "Performance of the P-band subsystem and the X-band interferometer of the F-SAR airborne SAR instrument," in *Proc. IEEE Int. Geosci. Remote Sens. Symp.*, 2012, pp. 5037–5040.

[51] K. R. Sørheim et al., "Characterization of low sulfur fuel oils (LSFO)—A new generation of marine fuel oils," SINTEF, Trondheim, Norway, Tech. Rep. OC2020 A-050, 2020.

Cornelius Patrick Quigley received the bachelor's degree in physics from the Department of Physics, National University of Ireland, Cork, Ireland, in 2013, the master's degree in sea ice remote sensing using SAR from the Department of Physics and Technology, UiT-The Arctic University of Norway, Tromsø, Norway, in 2017, and the Ph.D. degree in oil spill remote sensing using SAR from the Center for Integrated Remote Sensing and Forecasting for Arctic Operations, UiT-The Arctic University of Norway, Tromsø, Norway, in 2021.

His current research interests include remote sensing of ocean areas, specifically by polarimetric SAR and with a focus on marine oil pollution.

A. Malin Johansson (Member, IEEE) received the M.Sc. degree in physical oceanography from Gothenburg University, Gothenburg, Sweden, in 2005, and the Ph.D. degree in remote sensing from Stockholm University, Stockholm, Sweden, in 2012.

She is an Associate Professor with the Department of Physics and Technology, UiT-The Arctic University of Norway, Tromsø, Norway, which she joined in 2014. She was a Postdoctoral Researcher with Radar Remote Sensing Group, Department of Earth and Space Sciences, Chalmers University of Technology, Gothenburg, Sweden. Her research interests include multisensor remote sensing of sea ice, oil spills, and harmful algae blooms.

Cathleen E. Jones (Member, IEEE) received the B.S. degree from Texas A&M University, College Station, TX, USA, in 1982, and the Ph.D. degree from the California Institute of Technology, Pasadena, CA, USA, in 1991, both in physics.

She is a Senior Research Scientist with NASA Jet Propulsion Laboratory, California Institute of Technology, Pasadena, CA, USA, where her main research is focused on the development of methods for determining oil slick characteristics, monitoring subsidence and critical infrastructure, and understanding land building/loss in deltas. She is the Applications Co-Lead of NASA NISAR Science Team.

Benjamin Holt (Member, IEEE) received the B.A. degree in human biology from Stanford University, Stanford, CA, USA, in 1972, and the M.S. degree in physical oceanography from the University of Southern California, Los Angeles, CA, USA, in 1988.

He has been a Research Scientist with Ocean Circulation Group within Earth Science Section, Jet Propulsion Laboratory, California Institute of Technology, Pasadena, CA, USA, since 1978. His research interests include using multisensor remote sensing data to examine the geophysical state of polar sea ice and snow, coastal oceanography and circulation, and the detection of marine pollutants.